



Provided by the author(s) and University of Galway in accordance with publisher policies. Please cite the published version when available.

Title	Simulation of turbulent flow in a rapid compression machine: Large Eddy Simulation and computationally efficient alternatives for the design of ignition delay time experiments
Author(s)	Yousefian, Sajjad; Quinlan, Nathan J.; Monaghan, Rory F. D.
Publication Date	2018-07-05
Publication Information	Yousefian, Sajjad, Quinlan, Nathan J., & Monaghan, Rory F. D. (2018). Simulation of turbulent flow in a rapid compression machine: Large Eddy Simulation and computationally efficient alternatives for the design of ignition delay time experiments. <i>Fuel</i> , 234, 30-47. doi: <a href="https://doi.org/10.1016/j.fuel.2018.06.117">https://doi.org/10.1016/j.fuel.2018.06.117</a>
Publisher	Elsevier
Link to publisher's version	<a href="https://doi.org/10.1016/j.fuel.2018.06.117">https://doi.org/10.1016/j.fuel.2018.06.117</a>
Item record	<a href="http://hdl.handle.net/10379/10027">http://hdl.handle.net/10379/10027</a>
DOI	<a href="http://dx.doi.org/10.1016/j.fuel.2018.06.117">http://dx.doi.org/10.1016/j.fuel.2018.06.117</a>

Downloaded 2024-04-23T12:18:33Z

Some rights reserved. For more information, please see the item record link above.



# Simulation of Turbulent Flow in a Rapid Compression Machine: Large Eddy Simulation and Computationally Efficient Alternatives for the Design of Ignition Delay Time Experiments

*Sajjad Yousefian<sup>1,2,3,\*</sup>, Nathan J. Quinlan<sup>1,3</sup> and Rory F. D. Monaghan<sup>1,2,3</sup>*

<sup>1</sup>Mechanical Engineering, National University of Ireland, Galway, Ireland

<sup>2</sup>Combustion Chemistry Centre, National University of Ireland, Galway, Ireland

<sup>3</sup>Research Centre for Marine and Renewable Energy, Galway, Ireland

## **Abstract**

Rapid compression machines (RCMs) are widely used by the fuel research community to provide engine-relevant conditions to study ignition delay time (IDT), which is a crucial target for validating chemical kinetic mechanisms for fuels. Creviced piston heads are routinely used to ensure temperature homogeneity within the combustion chambers of RCMs. However, due to the exponential dependence of kinetic rate coefficients on temperature, homogeneity of the

---

\* s.yousefian2@nuigalway.ie

temperature field is vital for clear interpretation of results and identification of chemical kinetic mechanisms. The overall aims of this work are to (1) support operators of RCMs in ensuring that their devices achieve sufficient levels of in-chamber temperature homogeneity and (2) validate performance of a previously-developed correlation for temperature inhomogeneity in RCMs at different conditions. Large Eddy Simulation (LES) is conducted to resolve 3D unsteady structure of turbulent flow, throughout compression and long post-compression times, at two representative operating conditions in the NUI Galway RCM. Results show that at higher pressures, 3D LES temperature and velocity fields are well approximated by a previous 2D laminar model. At low pressures, 2D laminar and 3D LES agree well for flow during compression, but predict different evolution of roll-up vortices and temperature distribution after compression. However, across all conditions there is satisfactory agreement between 2D laminar and 3D LES results for global temperature inhomogeneity. Moreover, the previously developed correlation (based on 2D laminar simulations) for temperature inhomogeneity is found to agree with 3D LES to within  $\pm 20\%$ . Therefore, the correlation may be used for preliminary design and evaluation of RCMs and RCM experiments. We propose a framework for design of RCM experiments based on the use of correlations, supported by 2D laminar simulations, and finally 3D LES of selected cases for confirmation.

**Keywords:** Rapid compression machine (RCM); Ignition delay time (IDT); Large Eddy Simulation (LES); Roll-up vortex; Temperature inhomogeneity

## **Nomenclature**

Abbreviations

BOC	Beginning of Compression
C <sup>3</sup>	Combustion Chemistry Centre
CAD	Computer-Aided Design
CFD	Computational Fluid Dynamics
DKEM	Dynamic Subgrid Kinetic Energy Model
DNS	Direct Numerical Simulation
DOE	Design of Experiment
EOC	End of Compression
ICHEC	Irish Centre for High-End Computing
LES	Large Eddy Simulation
LH	Latin Hypercube
MCS	Monte Carlo Simulation
NIST	National Institute of Standards and Technology
NTC	Negative Temperature Coefficient
NUI Galway	National University of Ireland Galway
PIV	Particle Image Velocimetry
PLIF	Planar Laser-Induced Fluorescence
RANS	Reynolds-Averaged Navier–Stokes
RCM	Rapid Compression Machines
RNG	Re-Normalisation Group

SIMPLEC Semi-Implicit Method for Pressure Linked Equations-Consistent

Letters

<i>C</i>	Model Constant
<i>D</i>	Main Chamber Diameter
<i>E</i>	Entrance Channel Length
<i>H</i>	Crevice Length
<i>I</i>	Inlet Height of Entrance Channel
<i>J</i>	Outlet Height of Entrance Channel
<i>L</i>	Half of Clearance Length
<i>M</i>	Pope Criterion
<i>Pe</i>	Peclet Number
<i>Pr</i>	Prandtl Number
<i>Re</i>	Reynolds Number
<i>S</i>	Stroke Length
<i>T</i>	Temperature
<i>U</i>	Average Piston Velocity
<i>V</i>	Volume
<i>W</i>	Crevice Height
<i>a</i>	Crevice Volume Ratio
<i>b</i>	Aspect Ratio
<i>k</i>	Turbulent Kinetic Energy

$t$	Post-compression time
Subscripts	
0	End of Compression Time
$\infty$	Very Long Post-Compression Times
$c$	Compression
$cr$	Crevice
$f$	Filter
$i$	Initial
$l$	Laminar
$max$	Maximum
$p$	Predicted
$s$	Stroke Length
$sgs$	Subgrid-Scale
$tot$	Total
$w$	Wall
Superscripts	
*	Dimensionless
—	Average
Greek letters	
$\Delta$	Grid Size
$\beta$	Exponential Coefficient of Correlation

$\varepsilon$	Temperature Inhomogeneity Parameter
$\mu$	Eddy Viscosity/Expected value
$\delta$	Boundary Layer Thickness
$\nu$	Average Kinematic Viscosity
$\rho$	Density
$\sigma$	Standard deviation
$\tau$	Stress

## 1. Introduction

Rapid compression machines (RCMs) are extensively used for investigating combustion characteristics of fuels at low to intermediate temperatures and elevated pressures. These experimental facilities simulate the process of adiabatic compression and intend to provide an environment of uniform, controllable pressure and temperature to investigate fundamental combustion characteristics, such as ignition delay time, and to develop detailed chemical kinetic mechanisms. A test gas is enclosed in the RCM chamber and it is compressed by rapidly accelerated pistons. In actual operation, the compression of a test gas in an RCM is accompanied by an inhomogeneous temperature field after the compression stroke. This inhomogeneity is associated with the formation of a roll-up vortex on the piston face, and leads to inhomogeneous ignition of fuel. Post-compression conditions of temperature and pressure are typically in the range 700–1200 K and 1–6 MPa, and typical test times are in the region of 1–200 ms [1]. Computational fluid dynamics (CFD) simulation is an effective tool for comprehensive study of the aerodynamics and temperature in RCM. So far, several CFD studies have been conducted to

characterize flow fields for different RCMs, but the main focus has been on laminar and Reynolds Averaged Navier-Stokes (RANS) models, outlined in this brief overview. Refer to Goldsborough et al. [2] for a comprehensive review of advances in RCM studies.

Lee et al. [3] performed CFD simulations that modelled flow as laminar to study the effect of a piston crevice design to suppress vortex formation. Würmel et al. [4] implemented CFD models to optimize the piston head crevice for the NUI Galway RCM and determined new factors that are important when optimizing the piston head crevice design. The authors implemented laminar and  $k - \varepsilon$  turbulence models and found that the use of turbulence model had very little effect on simulation results. Mittal et al. [5] numerically and experimentally compared the resulting aerodynamics and temperature fields produced by creviced and flat pistons. Experiments were conducted using planar laser-induced fluorescence (PLIF) and CFD simulations conducted using laminar,  $k - \varepsilon$  and re-normalisation group (RNG) turbulence models. Overall computational results showed that the features of aerodynamics were better predicted by laminar calculations in comparison with RANS turbulence models, while the actual aerodynamic pattern was expected to be somewhere in between the laminar and turbulent model predictions. Mittal et al. [6] conducted CFD simulations using a laminar model for the ignition of n-heptane in an RCM with a creviced piston in order to assess the validity of the zero-dimensional modelling to predict ignition delay and negative temperature coefficient (NTC) behaviour. The authors showed that zero-dimensional simulated results may not always accurately predict total ignition delays under two-stage ignition conditions. Mittal et al. [7] studied performance of an RCM with a creviced piston over a range of operating conditions through laminar CFD simulations with systematic

demonstration of the effects of compressed gas pressure, temperature, stroke length, and piston-end wall clearance on altering vortex formation and temperature homogeneity inside the reaction chamber. Simulated results showed that as compressed gas pressure was reduced, the temperature homogeneity deteriorated due to the combined effect of thicker boundary layer and increased flow velocities. Mittal et al. [8] experimentally studied autoignition of iso-octane with and without crevice containment using a laminar model and showed that post-compression induced mass transfer to the crevice can lead to considerably longer ignition delays. Yousefian et al. [9] presented a simplified framework for the prediction of temperature inhomogeneity in RCMs using a laminar model. The approach was applicable to any RCM configuration and any gas mixture properties. A dimensionless measure of temperature inhomogeneity was defined and found to be primarily dependent on only three dimensionless parameters, the Peclet number  $Pe$ , chamber aspect ratio  $b$ , and crevice volume ratio  $a$ , in order of decreasing importance. A set of laminar CFD simulations was generated to develop a generic correlation for temperature inhomogeneity as a function of these three parameters and dimensionless post-compression time. Bourgeois et al. [10] studied the autoignition of the iso-octane by comparing zero-dimensional and RANS simulations of the Argonne RCM. The results indicated that turbulence may only exert a minor influence on the ignition delay time and RANS simulation results were similar to those of the zero-dimensional simulations. Ben-Houidi et al. [11] experimentally studied the internal aerodynamics and temperature distribution of a flat piston RCM using high-speed PIV and 2D PLIF. The results showed that a higher density level induces lower velocities in the vortices. Also, the comparison of the temperature and flow fields at end of compression (EOC) and 40 ms post-compression showed that vortices bring colder gases inside the chamber.

Banaeizadeh [12] used Large Eddy Simulation (LES) to simulate non-reacting and reacting turbulent flow with flat and crevice pistons for the Michigan State University (MSU) RCM. It was shown that the in-cylinder temperature values were more uniform when the creviced piston was used. The results of this study were limited to the end of compression (EOC) and 5 ms post-compression. Lodier et al. [13] used LES to simulate turbulence and combustion inside a compression machine described by Guibert et al. [14], in which a reactive mixture was rapidly compressed in a combustion chamber. The reactive mixture was passed through a converging section and a turbulence generating grid at the entrance to the combustion chamber. After comparing with experiments, the geometry used in the LES simulation was reduced by a factor of 4 and used for Direct Numerical Simulation (DNS). This downsizing was required due to the computational requirements of DNS. It was shown that three-dimensional vortex stretching plays a crucial role inside the chamber of compression machine. Schmitt et al. [15–18] used DNS to study the compression stroke in an engine-like geometry that was experimentally characterized by Morse et al. [19]. The authors provided highly detailed insight into the evolutions of velocity and thermal boundary layer structure [15], thermal stratification [16] as well as wall heat transfer phenomena [16,17] at a spatial and temporal resolution that cannot be obtained using current experimental methods. Mandanis et al. [20] used this DNS data to investigate the predictive capabilities of LES with respect to the wall heat transfer and thermal stratification during the compression stroke for the same geometry using STAR-CD. The results indicated that LES underestimates the wall heat flux and the thermal stratification in comparison with the DNS.

Grogan et al. [21] emphasized that heat transfer and turbulence can significantly affect the character of the ignition process and obfuscate the interpretation of chemical kinetic studies. By considering the competition between turbulent, chemical, and heat transfer effects, a regime diagram was developed in this study to guide RCM experiments. Ihme [22] studied potential sources of turbulence in an RCM, such as the filling process, corner vortices, boundary layer-generated turbulence, and turbulence production by compressive strain. The author developed a self-contained mathematical model that described the amplification of small-scale turbulence fluctuations during the RCM compression phase and the subsequent ignition process. The author emphasized that the relative contributions of potential sources of turbulence have so far not been experimentally quantified and are most likely dependent on facility design and operating conditions.

This literature review shows that the characterisation of turbulent flow in an RCM remains an open challenge. The dominant assumption for CFD studies in the literature is a laminar model which needs to be validated over different operating conditions. The main focus of above studies is on the end of compression or early post-compression times. However, characterisation of the flow field over the entire range of post-compression time (5-200 ms) is essential to study ignition delay times. Moreover, there is a need to characterize the performance of an operating RCM for a range of operating condition and crevice configuration to assess the level of temperature inhomogeneity using more computationally-efficient tools. Therefore, the objectives of this work are: (1) to characterize the in-chamber fluid velocity and temperature fields in the NUI Galway twin-piston RCM using a three-dimensional (3D) large eddy simulation (LES) approach, (2) to compare the post-compression temperature field predictions of axisymmetric two-dimensional

(2D) laminar and 3D LES approaches, (3) to compare post-compression temperature inhomogeneity predictions given by 2D laminar CFD, 3D LES CFD and a previously-developed correlation [9], and (4) to propose a computationally-efficient framework for RCM testing campaigns.

## **2. Numerical Approach**

### **2.1. NUI Galway RCM**

A simplified schematic view of the RCM at NUI Galway, which employs a twin piston design, is shown in Figure 1. A test gas is enclosed in the RCM chamber and it is compressed by rapidly accelerated pistons. Pneumatic drive chambers behind each piston drive the pistons forward during the compression stroke. The use of two pistons greatly reduces the compression time in comparison with one piston, and thereby minimizes heat loss and thermal boundary layer formation during the compression stroke. A section view of key parts of RCM including main chamber (in grey), compression sleeves (in blue), and piston plungers (in red) is shown in this figure at the beginning of compression (BOC) and the end of compression (EOC) including creviced piston head. Stroke length per piston is 168.17 mm, main chamber diameter is 38.2 mm, and half of clearance length is 14.48 mm. More details of RCM and crevice dimensions are shown in Figure 1.

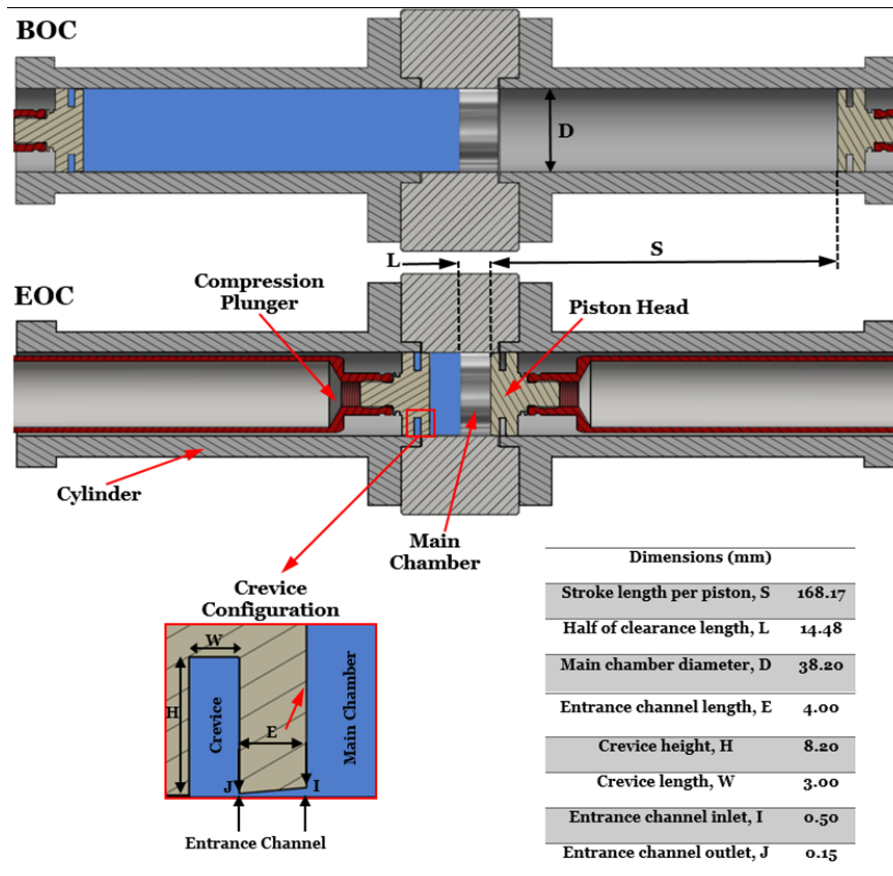


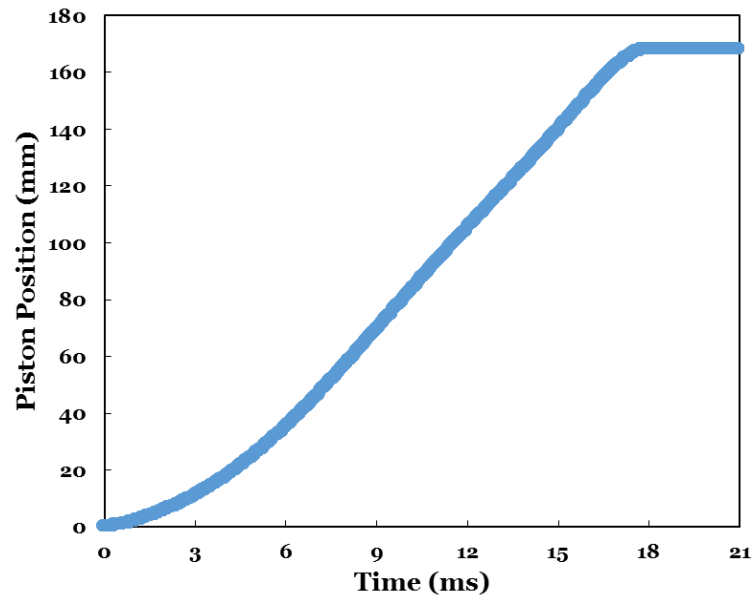
Figure 1: Simplified schematic view of the NUI Galway RCM in the BOC and EOC positions.

## 2.2. Computational Domain and Boundary Conditions

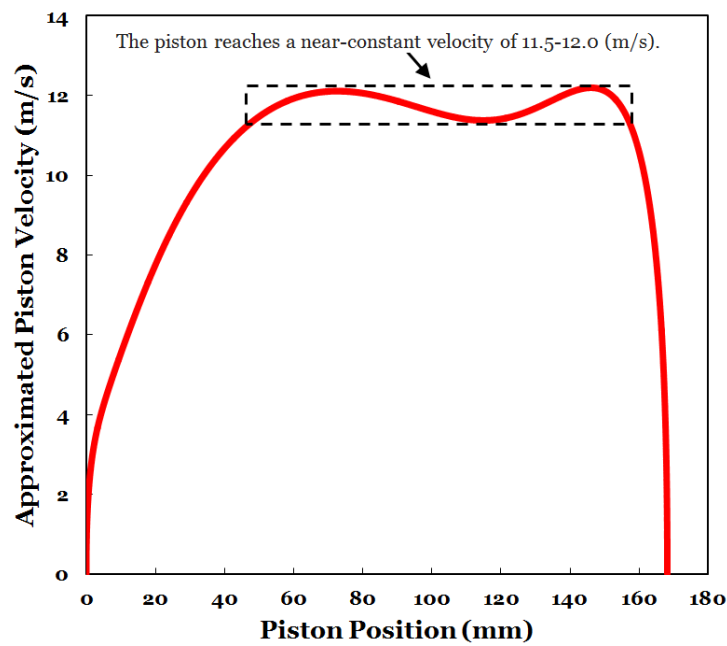
Cross-section views of the computational domain at the BOC and EOC are shown in Figure 1 (orange colour). While a two-dimensional axisymmetric computational domain was used in previous works [14] for a similar RCM, a full three-dimensional computational domain is used in this study due to the need to capture unsteady turbulent structures. The original CAD geometry

of the main chamber is cleaned-up and simplified by deleting the spurious details from numerical simulation point of view.

Although the RCM consists of two opposed pistons in a symmetrical arrangement, one piston has been considered in this study using the symmetry plane as a boundary condition at the middle of main chamber, which saves grid size and computational cost. Turbulence does not obey symmetry and the application of symmetry plane would therefore impose a constraint onto the resolved scales [23]. However, since the roll-up vortex, which is the main source of local flow instability, grows on the piston head, which is initially far from the symmetry plane, this simplification is deemed acceptable. The computational domain (orange colour) is divided to three zones in CFD simulations; the main chamber, entrance channel and crevice, as described in Figure 1. The piston and cylinder surfaces are modelled as isothermal no-slip walls at a temperature equal to the initial gas temperature. The piston motion is simulated using a profile based on experimental piston displacement. For post-compression times, the piston position is held constant. Experimental piston displacement as a function of time and approximated piston velocity (1<sup>st</sup> derivative of piston displacement) as a function of piston motion are shown in Figure 2.



(a)



(b)

**Figure 2: (a) Experimental piston displacement as a function of time and (b) Approximated piston velocity (1<sup>st</sup> derivative of piston displacement) as a function of piston position. Average piston velocity 9.34 (m/s), compression time 18 ms and stroke length 168.17 mm.**

### **2.3. Numerical Schemes and Simulation Cases**

Solving all scale levels of turbulence and simulation of the whole transition process including the development of disturbance waves, interaction between waves and boundary layers, ignition of turbulent spots, laminar flow breakdown, and development into fully turbulent is only possible in DNS [24]. However, LES as an alternative method for DNS uses the concept of solving the large-scale eddies directly, and modelling the small eddies. In this study the flow is simulated using ANSYS Fluent v16.0 using LES.

The subgrid-scale stresses resulting from the filtering operation in LES are unknown and require modelling. The original and dynamic Smagorinsky-Lilly models, are essentially algebraic models in which subgrid-scale stresses are parameterized using the resolved velocity scales. The underlying assumption is the local equilibrium between the transferred energy through the grid-filter scale and the dissipation of kinetic energy at small subgrid scales. Furthermore, using the Smagorinsky eddy viscosity approach [25] to model the small eddies create a major problem, as the transition onset location predicted by LES is sensitive to the value of Smagorinsky constant. The subgrid-scale turbulence can be better modeled by accounting for the transport of the subgrid-scale turbulence kinetic energy [26]. This model is more appropriate for predicting the transition onset, because the sub-grid eddy viscosity is automatically reduced to zero in a laminar boundary layer [24]. Therefore, the dynamic subgrid-scale kinetic energy model (DKEM) in ANSYS Fluent v16.0 based on the model proposed by Kim and Menon [27] and Kim [26] is used in this study. The subgrid-scale (sgs) kinetic energy ( $k_{sgs}$ ) is defined in Equation (1).

$$k_{sgs} = \frac{1}{2}(\overline{u_k^2} - \bar{u}_k^2) \quad (1)$$

The subgrid-scale eddy viscosity,  $\mu_t$  is computed using  $k_{sgs}$  in Equation (2) where  $\Delta_f$  is the filter-size computed from  $\Delta_f \equiv V_{cell}^{1/3}$ .

$$\mu_t = C_k \rho k_{sgs}^{1/2} \Delta_f \quad (2)$$

The subgrid-scale stress ( $\tau_{ij}$ ) can then be written in Equation (3).

$$\tau_{ij} - \frac{2}{3} \rho k_{sgs} \delta_{ij} = -2C_k \rho k_{sgs}^{1/2} \Delta_f \bar{S}_{ij} \quad (3)$$

$\bar{S}_{ij}$  is the rate-of-strain tensor for the resolved scale, which is determined directly from the gradient of the velocity field.

$$\bar{S}_{ij} \equiv \frac{1}{2} \left( \frac{\partial \bar{u}_i}{\partial x_j} + \frac{\partial \bar{u}_j}{\partial x_i} \right) \quad (4)$$

$k_{sgs}$  in the Equation (2) is obtained by solving the sgs kinetic energy transport equation.

$$\rho \frac{\partial \bar{k}_{sgs}}{\partial t} - \rho \frac{\partial \bar{u}_j \bar{k}_{sgs}}{\partial x_j} = -\tau_{ij} \frac{\partial \bar{u}_j}{\partial x_j} - C_\varepsilon \rho \frac{k_{sgs}^{\frac{3}{2}}}{\Delta_f} + \frac{\partial}{\partial x_j} \left( \frac{\mu_t}{\sigma_k} \frac{\partial k_{sgs}}{\partial x_j} \right) \quad (5)$$

In the above equations,  $\tau_{ij} = \rho \overline{u_i u_j} - \rho \bar{u}_i \bar{u}_j$  is the subgrid-scale stress and the model constants,  $C_k$  and  $C_\varepsilon$ , are determined dynamically and  $\sigma_k$  is set to 1.0 [26].

The Semi-Implicit Method for Pressure Linked Equations-Consistent (SIMPLEC) scheme is used for pressure-velocity coupling. A second order scheme for pressure is employed, along with second order upwind schemes for density, energy, and subgrid kinetic energy. Bounded central differencing for momentum; and a second order implicit method for the transient formulation of momentum are additionally used. Species transport is not considered as the flow is modelled as non-reacting. A maximum of fifty iterations were run per time step with criteria for globally-

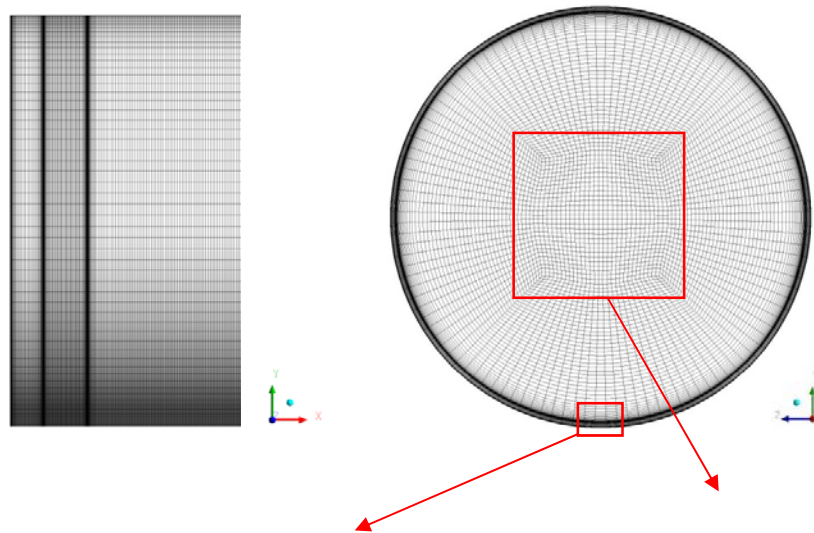
scaled residuals of  $10^{-3}$  for continuity, momentum and sub-grid kinetic energy, and  $10^{-6}$  for energy. Temperature-dependent gas thermophysical properties are evaluated by polynomials using the National Institute of Standards and Technology (NIST) database [28]. Simulations are carried out on Fionn, an Intel Xeon E5-based cluster at the Irish Centre for High-End Computing (ICHEC) [17].

In this study, seven LES simulations are conducted to study mesh sensitivity, the effects of operating conditions on flow regimes, and the assessment of temperature inhomogeneity correlation which was developed in previous study [9]. Three simulations are conducted for different mesh sizes at the initial pressure and temperature of 50 kPa and 298 K for nitrogen, which is described in detail in the mesh methodology section. The results of previous study [9] showed that various initial pressures resulted in different velocity and temperature distributions inside the RCM main chamber. Therefore, another simulation is conducted for the selected mesh at initial pressure and temperature of 100 kPa and 298 K for nitrogen to study the effect of operating conditions. Finally, three simulations at 50 kPa for minimum, average, and maximum Peclet numbers are conducted to assess the accuracy of the temperature inhomogeneity correlation [9] to predict LES results.

#### **2.4. Mesh Methodology**

The hexahedral mesh generation feature of ICEM CFD is used in this study to generate a structured mesh for the computational domain at the BOC shown in Figure 1. A blocking approach is implemented to construct 30 blocks and generate hexahedral elements inside the computational domain. The main chamber consists of two rectangular H-H blocks to avoid

singularities at the centreline, coupled with eight O-H blocks outside them, and eight O-O blocks close to walls. The entrance channel includes four O-O blocks and the crevice includes four O-H blocks coupled with four O-O blocks. As the piston moves, the mesh must conform to the decreasing volume of the domain. This is managed using the dynamic mesh layering scheme in ANSYS Fluent v16.0. The mesh as a whole translates with the piston, except for the layer of cells adjacent to the symmetry plane, which are reduced in axial length. As previously mentioned, the piston motion is simulated by the profile shown in Figure 2. When the length of these cells has decreased by a specified ratio, they are merged with the full-size cells in the next layer. This method allows the mesh in the area of most complex flow (near the piston) to remain constant, and results in faster computation due to the decrease in number of cells as compression proceeds. The mesh topology for the EOC and more detailed views for mesh number 2, which will be discussed in next section, are shown in Figure 3.



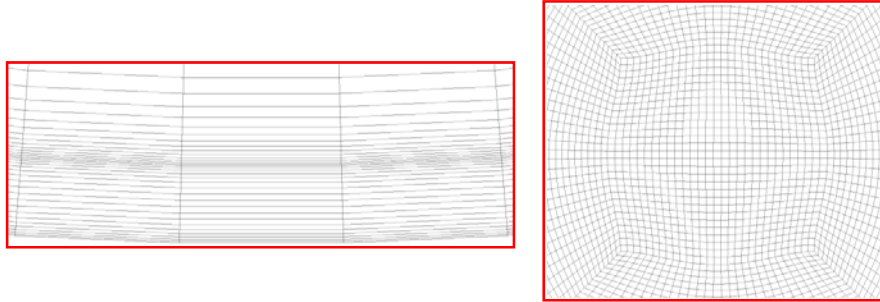


**Figure 3: Computational mesh number 2 at the EOC.**

## 2.5. Mesh Sensitivity Analysis

According to Pope's criterion [23,29], the quality of LES depends on the ratio of resolved turbulent kinetic energy ( $k_{res}$ ) to total  $k$ ,  $k_{tot}$ . This criterion assumes that  $k_{res}$  should account for at least 80% of  $k_{tot}$ . The ratio between  $k_{res}$  and  $k_{tot}$  is defined as  $M$  or Pope's criterion which is shown in Equation (6). This means that the computational mesh must be fine enough to enable a portion defined by  $M$  of the  $k$  in the domain to be resolved as opposed to modelled at the subgrid-scale (sgs).  $k_{sgs}$  represents subgrid-scale turbulent kinetic energy.

$$M = \frac{k_{res}}{k_{tot}} = \frac{k_{res}}{k_{sgs} + k_{res}} \quad (6)$$

A survey of LES simulation studies for internal combustion engine applications shows that some researchers, such as Di Mari et al. [30] and Wang et al. [31], used the value of 80% for Pope's criterion, while others, such as Bottone et al. [32] and Wang et al. [33], used 70%. Three computational meshes with different sizes are generated as described in Table 1 using the blocking method described above.

**Table 1. Comparison of three sets of meshes.**

<b>Mesh number</b>		<b>1</b>	<b>2</b>	<b>3</b>
<b>Number of mesh elements</b>	BOC	937,650	2,427,880	3,770,520
	EOC	460,750	1,109,801	1,703,481
<b>Average cell size at EOC <math>\Delta</math> (mm)</b>		0.510	0.358	0.297
<b>Computational cost (CPU-hours)</b>		5,832	15,024	41,952

Three simulations at initial pressure and temperature of 50 kPa and 298 K for nitrogen are conducted to evaluate Pope's criterion using these meshes. The impact of mesh size on Pope's criterion  $M$  over the whole 200 ms post-compression time inside the main chamber is plotted in Figure 4. This figure shows that mesh number 3 can resolve the highest proportion of kinetic energy, but its computational cost is extremely high, as indicated in Table 1. The results show that mesh number 2 is adequate and computationally efficient enough to capture the detailed structure of the velocity field over a wide range of post-compression times in which the turbulence levels are high. Furthermore, the distributions of  $M$  inside the crevice and entrance channel for mesh number 2 are shown in Figure 4. Therefore, mesh number 2 is selected for the LES simulations in this study. At the end of compression (post-compression time=0), the value of Pope's criterion for mesh number 2 is almost 26.3% bigger than mesh number 1 (coarse mesh) and 4.6 % lower than mesh number 3 (fine mesh). Therefore, using mesh number 1 and corresponding filter size grid considerably affects resolving the turbulent length scales at the end of compression.

As mentioned in the introduction section, Banaeizadeh [12] used LES to simulate the MSU RCM. To the authors' knowledge, this is the only available LES simulation for a practical and operating RCM in the literature. This study was limited to EOC and 5 ms post-compression time. It employed a mesh size of 572,920 elements and was implemented for stroke and bore dimensions of 254 mm and 50 mm, respectively. The working fluid was pure nitrogen with initial temperature and pressure of 297 K and 0.93 bar, respectively, which is close to the higher pressure initial condition in this study. The results of LES simulation for creviced configuration in this study using this mesh size was in satisfactory agreement with experimental temperature data. Although the NUI Galway RCM has considerably smaller dimensions of 168.2 mm and 38.2 mm for stroke and bore, a finer mesh of 2,427,880 elements (mesh number 2) has been used in this study. Moreover, Goryntsev et al. [34] and Bottone et al. [32] proposed that a mesh with average cell size  $\Delta \approx 1$  mm seems to be the minimum required to represent the flow field for internal combustion engine applications with reasonable accuracy. In general, the bore dimension for practical internal combustion engines is bigger than the NUI Galway RCM. Therefore, mesh sizes with average cell size of smaller than  $\Delta \approx 1$  mm are selected for the simulation of this machine as shown in Table 1.

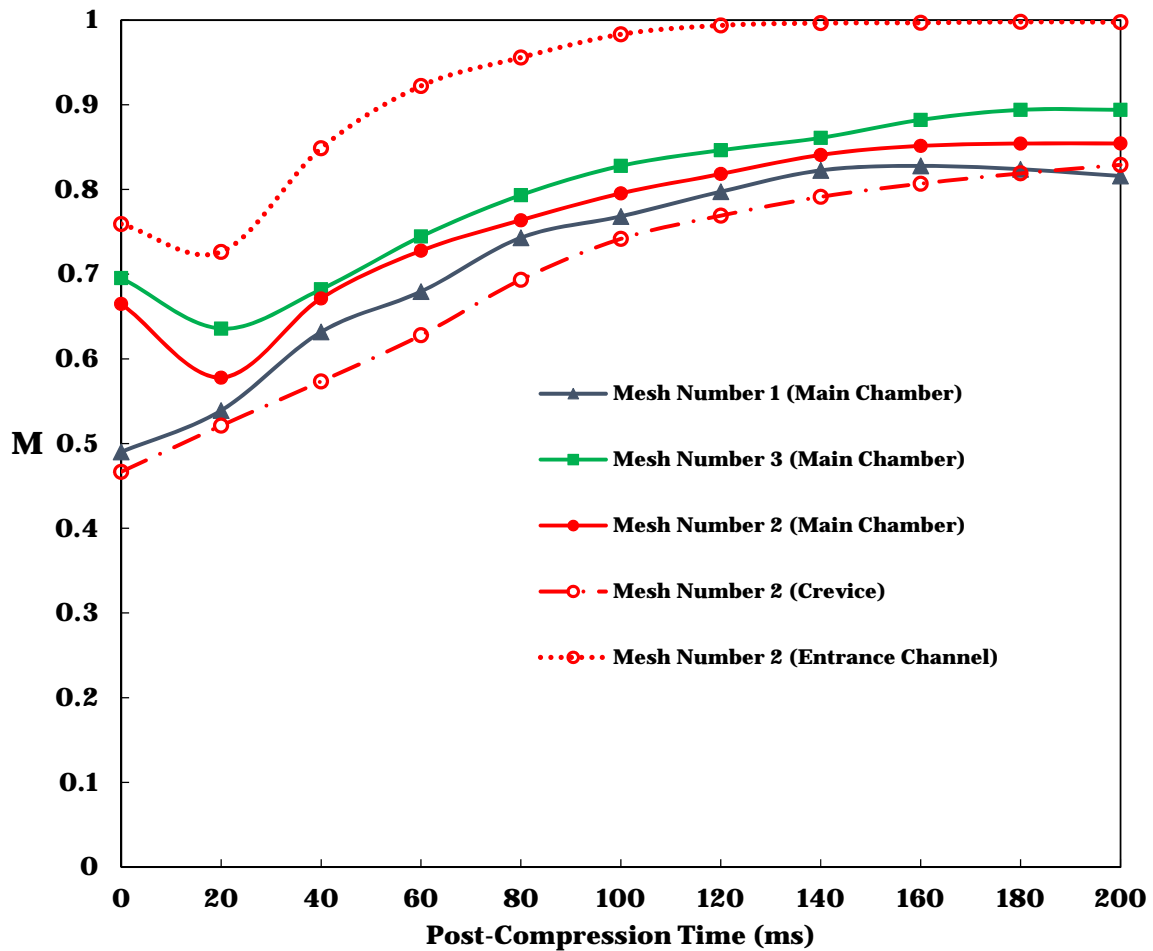
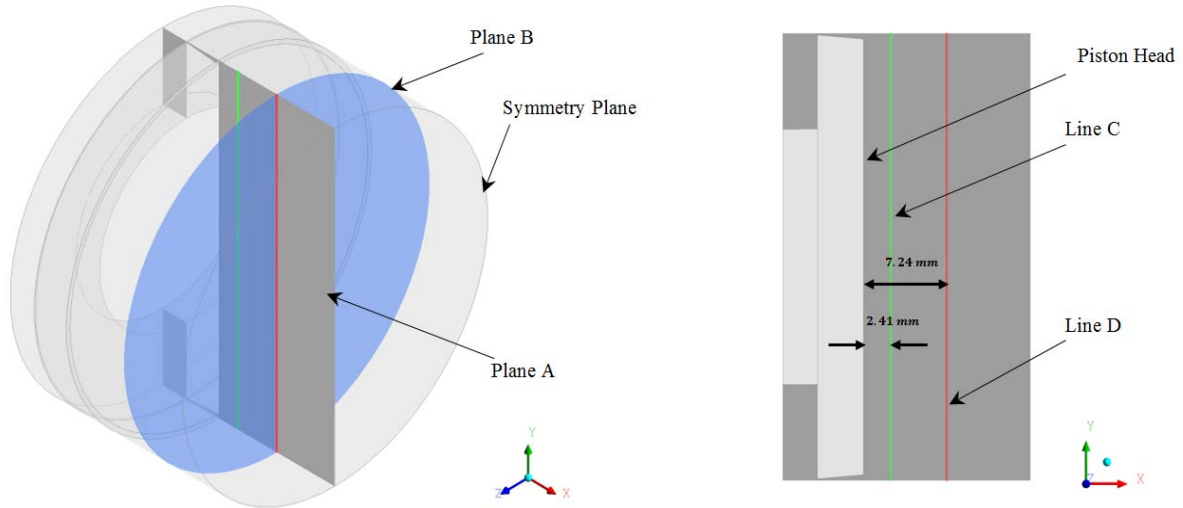


Figure 4. Evolution of  $M$  during post-compression for different mesh sizes.

### 3. Results and Discussion

The results of LES simulations using computational grid number 2 are presented in this section. The main focus within the computational domain for this analysis is the main chamber during long post-compression times. Figure 5 shows planes A and B inside the computational domain which are selected for post-processing. Plane A is the middle plane across main chamber, entrance channel, and crevice perpendicular to  $z$  axis. Plane B is middle plane inside main chamber perpendicular to  $x$  axis. Moreover, two lines are selected inside the main chamber

to show the distribution of selected flow field variables. As shown in Figure 5, line C is close to the piston head and line D is located at the middle of main chamber after EOC.



**Figure 5: Representation of planes and lines inside the computational domain to show the distribution of flow field variables.**

### 3.1 Effects of Initial Pressure

Figure 6 shows total temperature distribution on planes A and B at the 0 ms (EOC), 50 ms, 100 ms, 150 ms, and 200 ms post-compression times for the high pressure ( $P_i = 100$  kPa,  $P_{EOC} = 2639$  kPa) case. The maximum temperature in the chamber is 740 K for this case occurs at EOC. The result at EOC shows that crevice design is able to effectively capture the thermal boundary layer during compression and there is no roll-up vortex on the piston face. Previous work [9] showed that for an older crevice design, with a volume of 12% smaller than the current design, there was still a vortex on piston face at EOC at similar condition. At this time, thermal boundary layer thickness is very small compared to the main chamber diameter. At 50 ms post-

compression time, the temperature field has still a well-controlled homogenous core. Due to heat transfer at the isothermal wall, temperature decreases and thermal boundary layer thickness increases, as shown on plane B. For longer post-compression times of 100 and 150 ms, temperature throughout the main chamber is mostly homogeneous, with a few regions of low temperatures, as shown on plane B. At a very long post-compression time of 200 ms, the thermal boundary layer has maximum thickness, and the volumes of regions with lower temperatures at the core region of main chamber are increased.

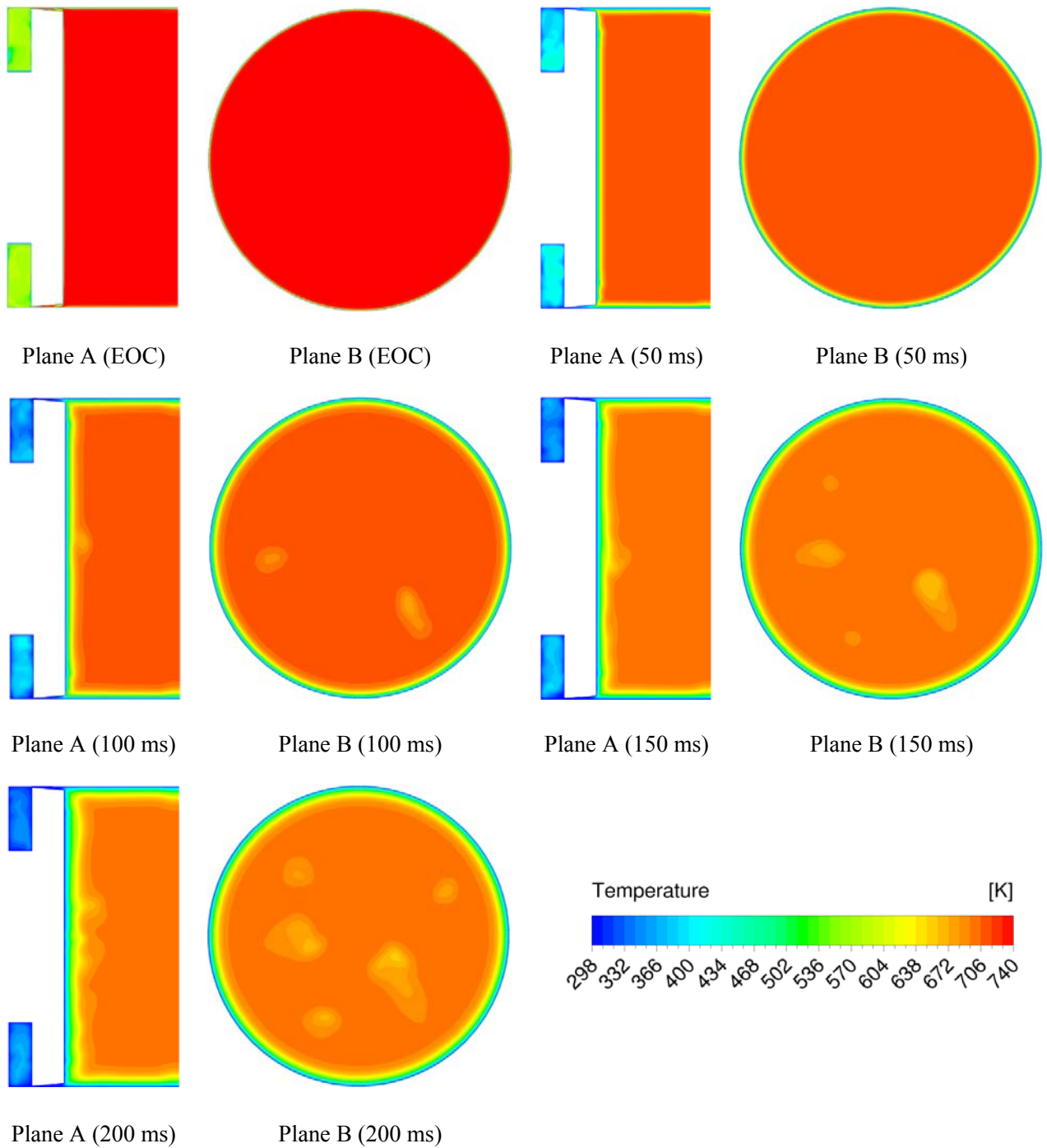


Figure 6: LES computed total temperature distributions at the high-pressure reference condition during post-compression times on planes A and B. Nitrogen, compression time 18 ms, initial pressure 100 kPa, initial temperature 298 K.

In general, the RCM at this condition has a satisfactory performance with regard to temperature homogeneity and there is no roll-up vortex mixing effects even for long post-compression times. The main source of turbulence at long post-compression times (more than 100 ms) for this condition is boundary layer generated turbulence. Ihme [22] emphasized the role of this mechanism to generate turbulent flow field in RCMs. Boundary layer generated turbulence is limited to the region close to piston head.

Figure 7 shows velocity vector distribution (plane A and B) at the high-pressure reference condition for 0-200 ms post-compression times. The velocity vector distribution inside the entrance channel and crevice, which are almost two order of magnitude higher than in the main chamber, are not shown in this figure for reasons of clarity. This figure shows that for this condition, velocity magnitude inside the main chamber has small values during the post-compression time, relative to the average piston speed ( $\sim 10$  m/s). At the EOC there is flow from the main chamber to the entrance channel of the crevice with a maximum velocity magnitude of 0.74 m/s. The velocity vector distribution close to the chamber walls shows that during all post-compression times, the flow direction is from main chamber to the entrance channel. This shows the capability of crevice to accommodate boundary layer flow during the compression time and even post-compression times, due to the cooling of the crevice gas. Therefore, there is no roll-up vortex on the piston face. At 150 ms and 200 ms post-compression times there are eddies with low velocity magnitudes inside the main chamber corresponding to low temperature regions as shown on plane B.

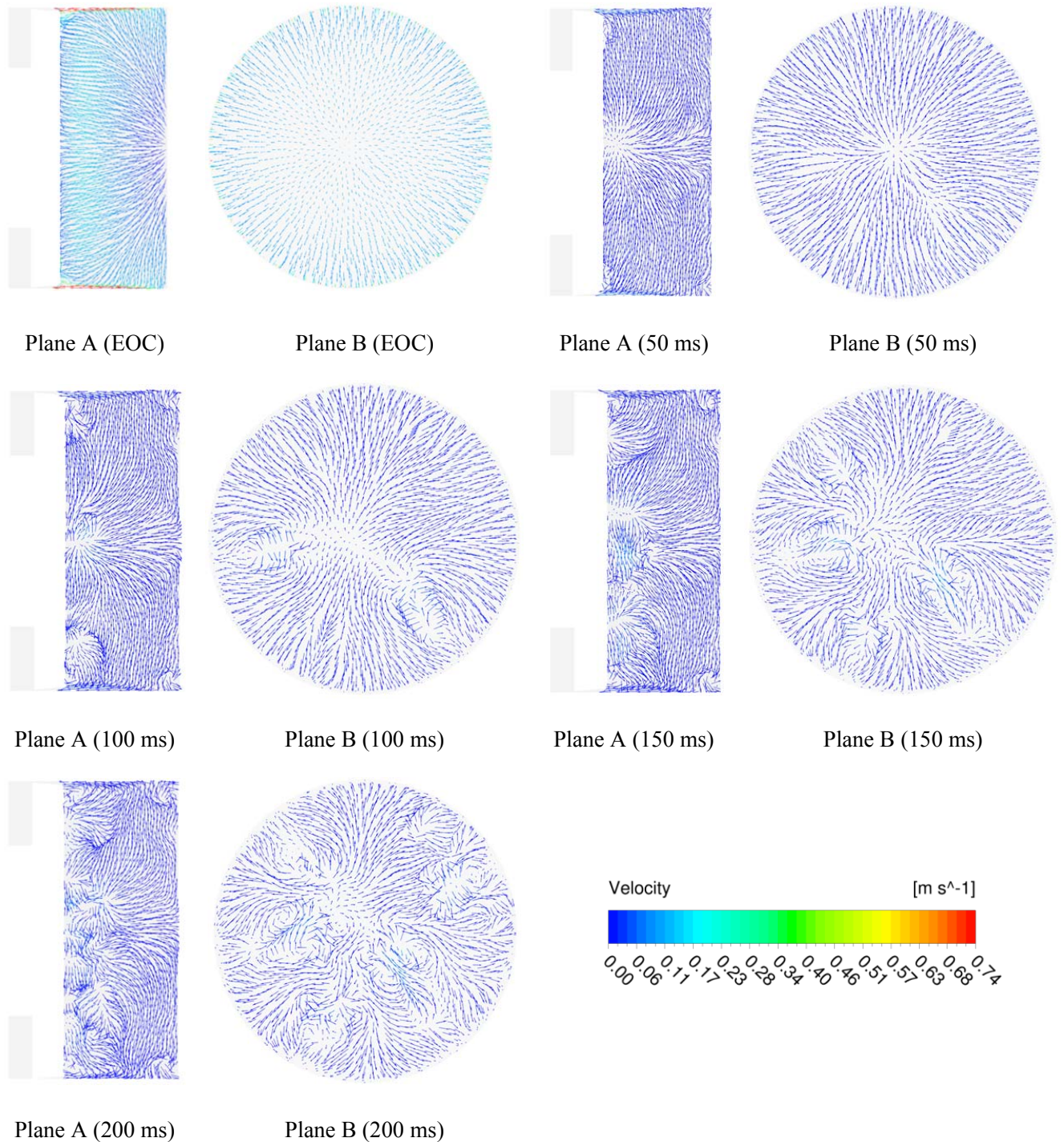


Figure 7: LES computed velocity vector distribution (planes A and B) and corresponding instantaneous

**streamlines (Plane B) at the high-pressure reference condition during post-compression times. Nitrogen, compression time 18 ms, initial pressure 100 kPa, initial temperature 298 K. The crevice is not shown.**

Figure 8 shows total temperature distribution on planes A and B at the EOC, 50 ms, 100 ms, 150 ms, and 200 ms post-compression times for the low pressure ( $P_i = 50$  kPa,  $P_{EOC} = 1293$  kPa) reference case. Although a considerable amount of boundary layer flow is captured during compression, there is small roll-up vortex on the piston face at EOC seen on plane A. At 50 ms, in contrast to the high pressure case, almost the entire volume of the main chamber is occupied by the growing roll-up vortex. Turbulent eddy structures appear inside the main chamber due to this mechanism at this time as shown on plane B. At 100 ms post-compression time this vortex is mixing with the thermal boundary layer, which considerably increases the level of temperature inhomogeneity by bringing cold boundary layer gas into the core. The overall phenomenon was previously predicted using a 2D laminar axisymmetric model [9]. However, the LES model helps to characterize eddy structures with different length scales, which the 2D laminar axisymmetric model failed to predict. At longer post-compression times of 150 and 200 ms, turbulent eddy structures are completely distributed inside the main chamber. Turbulent eddy structures are scattered over the entire volume with different length scales. The values of temperature for these turbulent eddies are lower than the core regions, which further increases temperature non-uniformity.

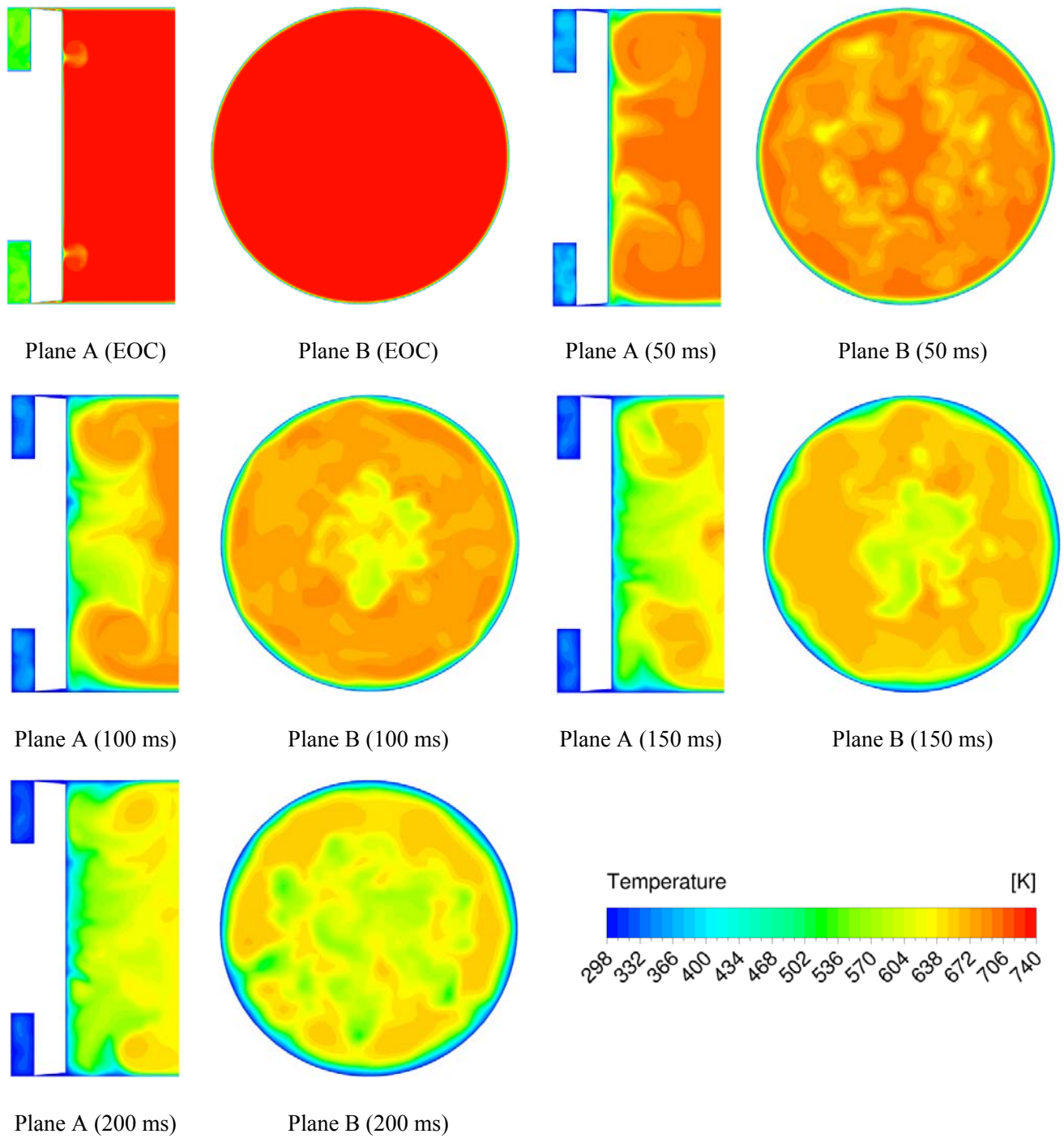


Figure 8: LES computed temperature distribution at the low-pressure reference condition during post-

**compression times. Nitrogen, compression time 18 ms, initial pressure 50 kPa, initial temperature 298 K.**

Park and Keck [35] developed a criterion for a well-defined adiabatic core in a designed RCM. The Authors prescribed that for the type designed and constructed in their experiment, the Reynolds number based on piston speed  $U$ , stroke length  $S$  and average kinematic viscosity during the compression time  $\nu$  requires a value less than  $10^5$  to keep all boundary layers laminar. Under these conditions the laminar boundary layer thickness is given by [35]:

$$\delta_l = \sqrt{\alpha t_q} \quad (7)$$

Where,  $\alpha$  is average thermal diffusivity during the compression time and  $t_q$  is cooling time [35]. According to the Park and Keck [35], for a well-defined adiabatic core in the developed RCM, the laminar boundary layer thickness to the clearance length ( $\delta_l/L$ ) should be less than  $\sim 0.1$ . The average thermal diffusivity during the compression time is calculated using 3D LES simulations at high and low initial pressure conditions to estimate the parameter ( $\delta/L$ ) during post-compression times for the NUI Galway RCM and the results are shown in Table 2. The results show that the values of ( $\delta/L$ )  $< 0.1$  for most post-compression times at high initial pressure condition and  $> 0.1$  for most post-compression times at low initial pressure condition. Based on the computed results using 3D LES in Figure 6 and Figure 8, there is a well-controlled homogeneous core during post-compression times at high initial pressure condition and a perturbed core at low initial pressure conditions. Therefore, the predicted results using the criterion developed by the Park and Keck [35] are in agreement with the computed results by 3D LES.

**Table 2. Comparison of values for the criterion developed by Park and Keck [35] at high and low initial pressure conditions using 3D LES simulations in the NUI Galway RCM.**

Post-Compression time (ms)	$\delta/L$	$\delta/L$
	(High initial pressure)	(Low initial pressure)
50	0.057	0.080
100	0.081	0.114
150	0.099	0.140
200	0.115	0.162

The structures of these turbulent eddies are visualized in Figure 9 using velocity vector distributions on planes A and B and the corresponding path lines on plane B. At EOC the velocity magnitude is considerably higher in comparison to the high-pressure condition (Figure 7). At 50 ms post-compression time, there are streamlines with maximum velocity magnitude of 0.74 m/s approaching to core of main chamber and forming eddy structures. At 100 ms post-compression there are turbulent eddies with different length scales close to the wall. The presence of these eddies confirms the interaction of roll-up vortex and boundary layer, which intensifies the level of temperature inhomogeneity. At 150 and 200 ms post-compression times, thermal boundary layers are swept into the main chamber core by eddies with high length scale due to mixing with roll-up vortex. At these times, there are high intensity turbulent eddies with various length scales present in the core, as shown on plane B.

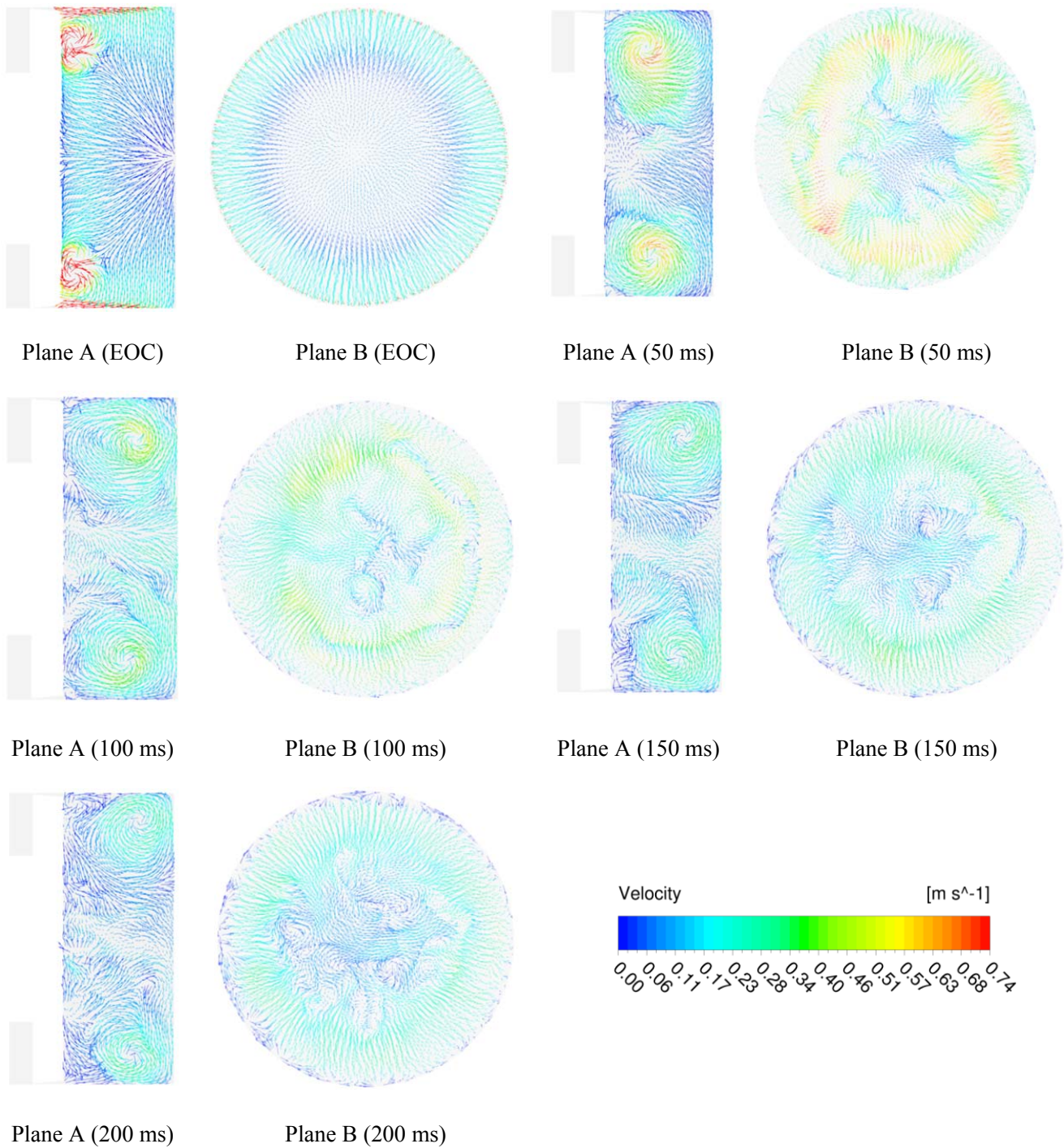


**Figure 9:** LES computed velocity vector distribution (planes A and B) and corresponding instantaneous streamlines (Plane B) at the low-pressure reference condition during post-compression times. Nitrogen,

**compression time 18 ms, initial pressure 50 kPa, initial temperature 298 K. The crevice is not shown.**

Figure 10 and Figure 11 show the comparison of total temperature distribution along line C, close to piston face, and line D, at the middle of main chamber, for the high-pressure (solid lines) and low-pressure (dashed lines) reference cases at post-compression times of 50 ms (blue lines) and 200 ms (red lines). Figure 10 shows that for the high initial pressure condition at 50 ms post-compression there is a well-controlled temperature distribution. However, this temperature distribution is disturbed due to the spatial inhomogeneity at 200 ms. For the low-pressure condition at 50 ms, there is a lower magnitude, non-uniform and non-symmetric temperature distribution due to the mixing effects of the roll-up vortex. At 200 ms, there is a turbulent flow close to the piston face with a perturbed spatial distribution for velocity vectors as shown in Figure 7 and Figure 9. Therefore, the temperature distribution on line C, which is close to the piston face, is chaotic with fluctuations for both low and high initial pressure conditions. The same behaviour is observed at a different spatial location in Figure 11.

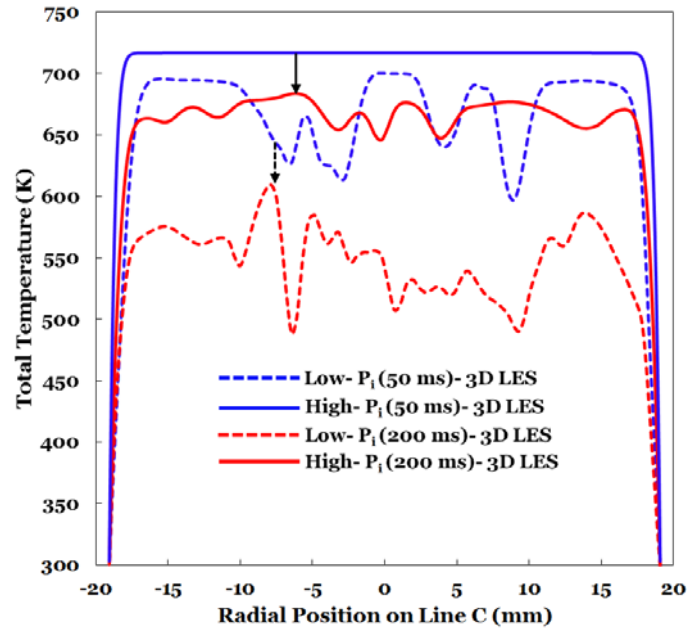


Figure 10: Comparison of computed temperature distribution along line C for high-pressure (solid lines) and low-pressure (dashed lines) reference cases at post-compression times of 50 ms (blue lines) and 200 ms (red lines).

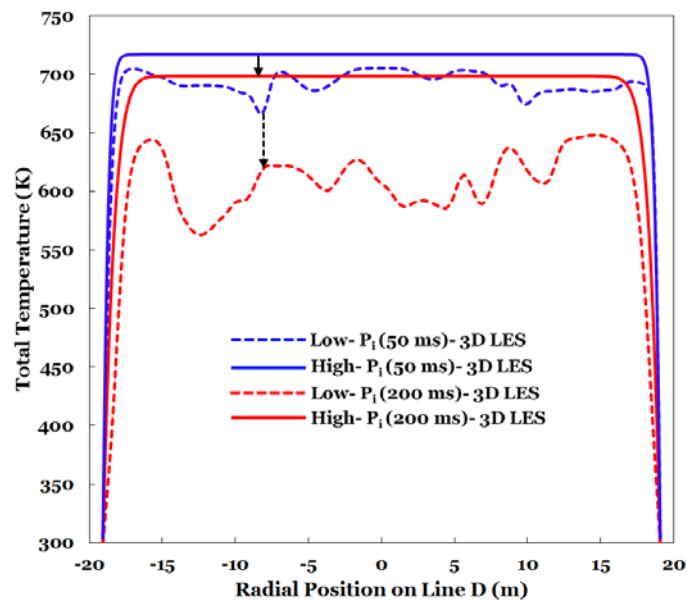


Figure 11: Comparison of computed temperature distribution along line D for high-pressure (solid lines) and low-pressure (dashed lines) reference cases at post-compression times of 50 ms (blue lines) and 200 ms (red lines).

### **3.2. Comparison of LES and 2D Laminar Models**

As described previously, the main focus of the literature to date has been on using the laminar approximation in CFD simulations. This section performs a full comparison of LES and 2D laminar results. In previous work by the authors [9], a 2D laminar model was implemented for the same RCM configuration but with a different crevice design. A set of 2D laminar and 3D LES CFD simulations are conducted in this study for the high and low initial pressure conditions using the current crevice design. The simulation setup for 2D laminar case is described in previous study [9]. The computational grid for 2D laminar model is almost 60 times smaller than mesh number 2, which is implemented for LES simulations.

A comparison for mass-weighted average of total pressure inside the main chamber of RCM as a function of time using both LES and 2D laminar models at high and low initial pressure conditions is shown in Figure 12. The results show that there is a good agreement between the 3D LES and 2D laminar models over the compression and post-compression times at both high and low initial pressure conditions.

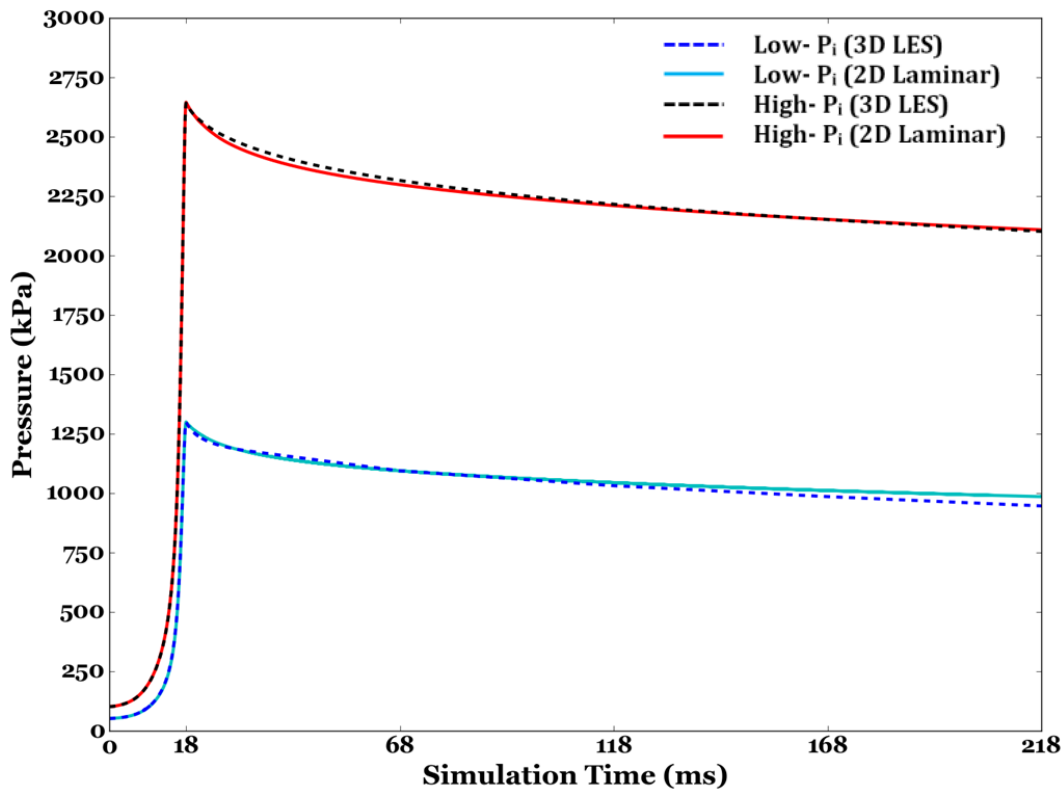
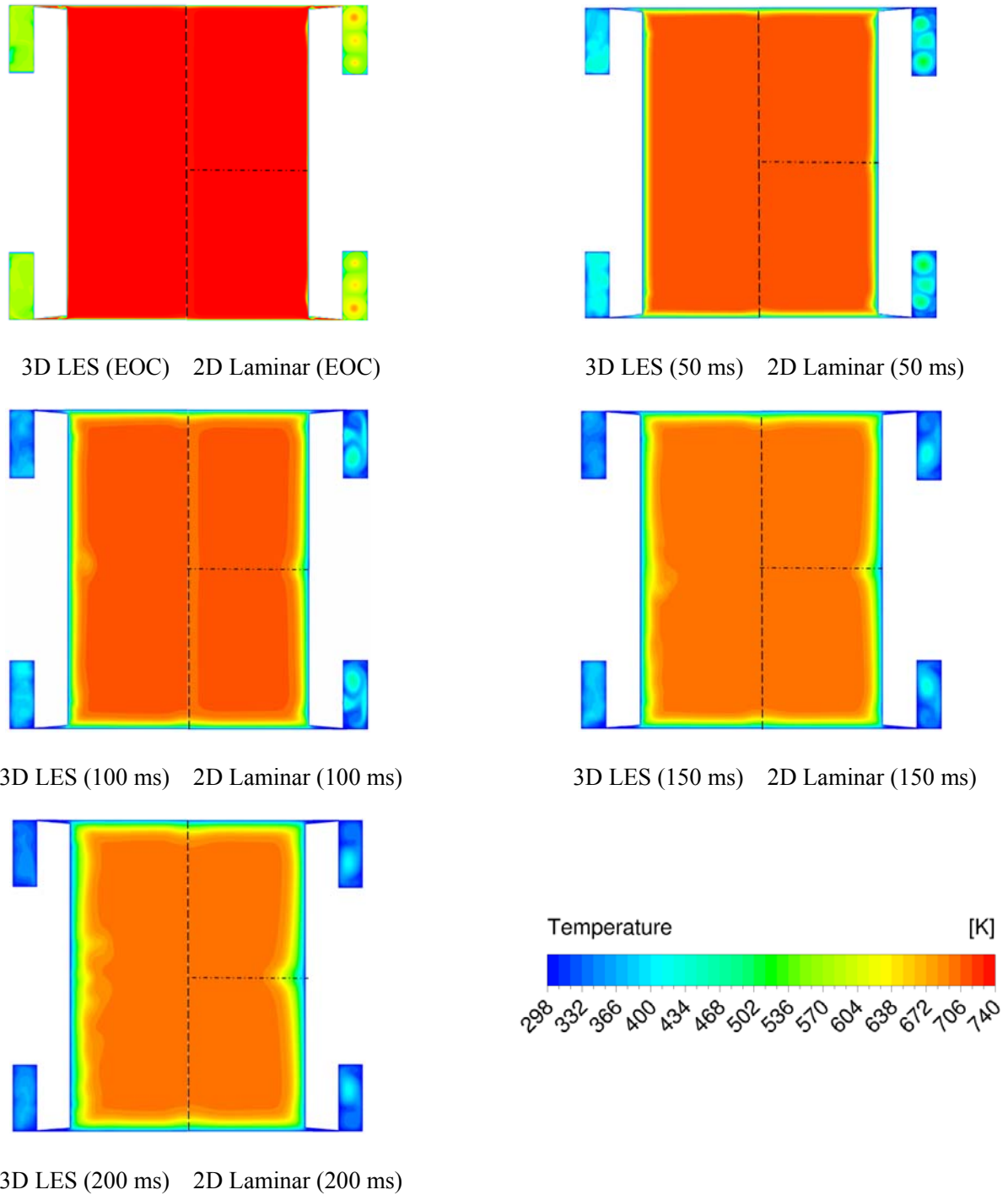


Figure 12: Comparison of computed mass-weighted average of pressure inside the main chamber of RCM using 2D laminar axisymmetric [9] (dashed lines) and LES (solid lines) at low and high initial pressure conditions. Nitrogen, compression time 18 ms, post-compression time 200 ms, initial pressures 50 and 100 kPa, initial temperature 298 K.

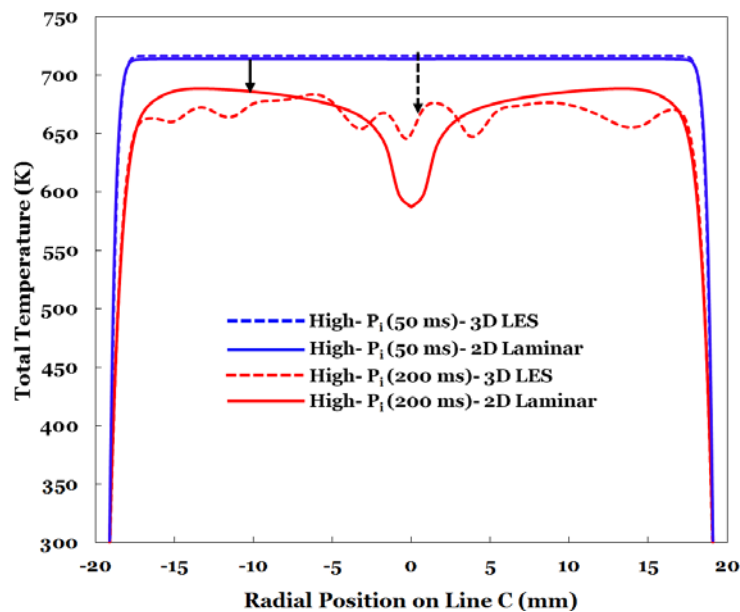
The comparison of temperature distribution for LES and 2D laminar cases at EOC and post-compression times for high initial pressure condition is presented in Figure 13. This figure confirms that at high pressures, the 2D laminar axisymmetric model gives results very close to LES. It can therefore be stated that under these conditions, laminar modelling can be used instead of LES. The computational cost for one 2D laminar simulation is 356 CPU-hours, which is  $\sim 42$  times lower than that for LES. As discussed in the previous section, boundary layer generated turbulence is important in the absence of a roll-up vortex.



**Figure 13: Comparison of computed total temperature distribution for LES and 2D laminar axisymmetric [9]. Nitrogen, compression time 18 ms, initial pressure 100 kPa, initial temperature 298 K. Left side of dashed line shows LES results and right side of dashed line shows 2D laminar result. Horizontal dash-dot**

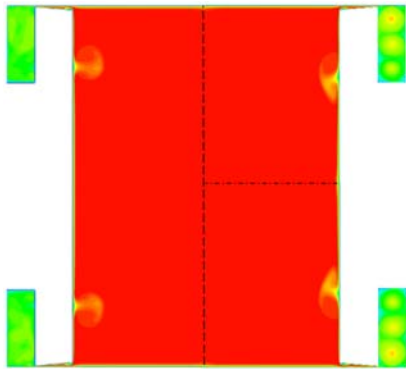
**line represents symmetry line for 2D laminar result.**

Figure 14 shows the radial distribution of temperature on line C close to the piston head for LES and 2D laminar cases at 50 ms and 200 ms post-compression times. This figure shows that there is an agreement between the 2D laminar and 3D LES models at 50 ms post-compression and there are no temperature fluctuations or roll-up vortex close to piston face. The contrast between the predictions of laminar and LES models is obvious at 200 ms. For the LES case, non-uniform temperature distribution is present close to piston face due to the fluctuations in the boundary layer. For the laminar case, there is a well-controlled temperature distribution and a considerable under-prediction for the temperature magnitude at the centreline.

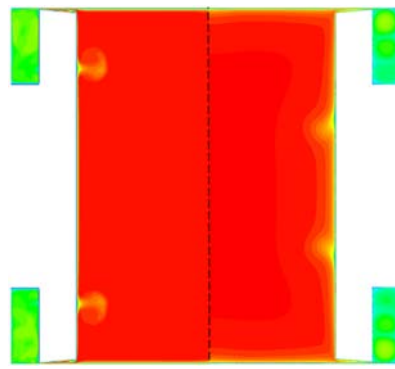


**Figure 14: Comparison of computed temperature distribution along line C using 2D laminar axisymmetric [9] (solid lines) and LES (dashed lines) models at post-compression times of 50 (blue lines) and 200ms (red lines) for high-pressure condition.**

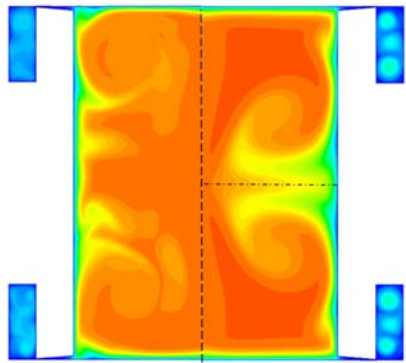
Figure 15 shows the comparison of LES and 2D laminar cases for the low-pressure condition at the end of compression and during the post-compression times. Furthermore, the comparison of LES and URANS ( $k - \omega$  SST) for temperature distribution is shown at the end of compression. The simulation of URANS ( $k - \omega$  SST) model is conducted using mesh number. The position of roll-up vortex on piston face using 2D laminar model is slightly bigger and closer to the centreline of main chamber due to different prediction of radial velocity in comparison with the 3D LES. However, the predicted roll-up vortex on piston face using URANS ( $k - \omega$  SST) is highly dissipated at the end of compression in comparison with the 3D LES. Therefore, there is a better prediction for the roll-up vortex on piston face in 2D laminar model in comparison with the 3D URANS ( $k - \omega$  SST).



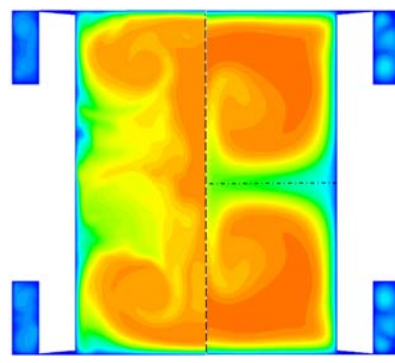
3D LES (EOC) 2D Laminar (EOC)



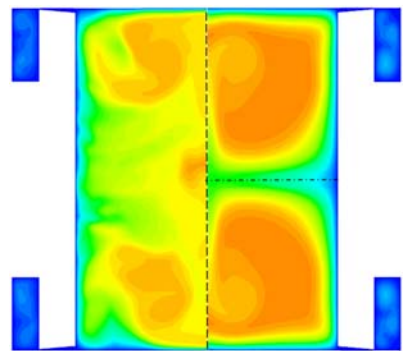
3D LES (EOC) 3D (k -  $\omega$  SST) (EOC)



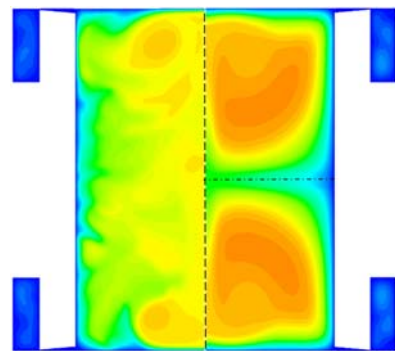
3D LES (50 ms) 2D Laminar (50 ms)



3D LES (100 ms) 2D Laminar (100 ms)



3D LES (150 ms) 2D Laminar (150 ms)



3D LES (200 ms) 2D Laminar (200 ms)

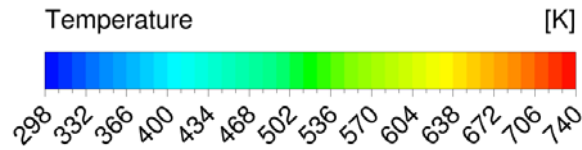


**Figure 15: Comparison of computed total temperature distribution for LES, 2D laminar axisymmetric[9] and 3D URANS ( $k - \omega$  SST). Nitrogen, compression time 18 ms, initial pressure 50 kPa, initial temperature 298 K. Left side of dashed line shows LES results and right side of dashed line shows 2D laminar result. Horizontal dash-dot line represents symmetry line for 2D laminar result.**

As described, the position of roll-up vortex on piston face in the 2D laminar model is different in comparison with the 3D LES at the end of compression. The role of crevice at the end of compression is important for this difference. At the low initial pressure condition, the flow inside the crevice is fully turbulent and the mass-weighted average velocity magnitude inside the crevice for 2D Laminar and 3D LES models are 23.30 m/s and 12.83 m/s, respectively. In addition to the axial and radial components, the 3D LES model is able to resolve the tangential component of velocity as well as the three-dimensional structures inside the crevice. This is not possible with the 2D laminar model. Resolving the tangential component and 3D structures of turbulent eddies considerably change the velocity distribution and magnitude inside the crevice for 3D LES in comparison to the 2D laminar model. There is a simple and relatively steady structure of the flow in the 2D laminar model. However, in the 3D LES model there is an unsteady, irregular and asymmetrical pattern for the velocity distribution which is different at each time step and dominated by the motion and evolution of small eddies and three-dimensional structures.

As shown in Figure 15, during post-compression times, temperature distributions are different for LES and 2D laminar due to the failure of 2D laminar model to predict highly turbulent eddies with lower temperatures inside the main chamber. The results confirm the deficiency of the 2D

laminar model to predict exact flow field inside the main chamber during post-compression times in the case of there being a roll-up vortex on the piston face at EOC. Also, the laminar model fails to predict the propagation of turbulent eddies from the thermal boundary layer into the core of the main chamber. Therefore, the simplifications inherent to the 2D laminar model, such as two-dimensional computational domain, low grid resolution, and the assumption of laminar flow, influence the capability of model to predict the flow field.

At 50 ms post-compression in Figure 15, the position of roll-up vortex is closer to the centreline in the 2D laminar model than in LES. The profile of radial velocity along the line C close to piston face is shown in Figure 16 at this time. In this figure, the positions of maximum velocity magnitude correspond to the roll-up vortex on piston face. For the laminar model these positions are close to the centreline, with different magnitude in comparison with LES model. Moreover, there is a non-uniform distribution of radial velocity for LES model which shows the distribution of turbulent eddies as well as roll-up vortex on piston face.

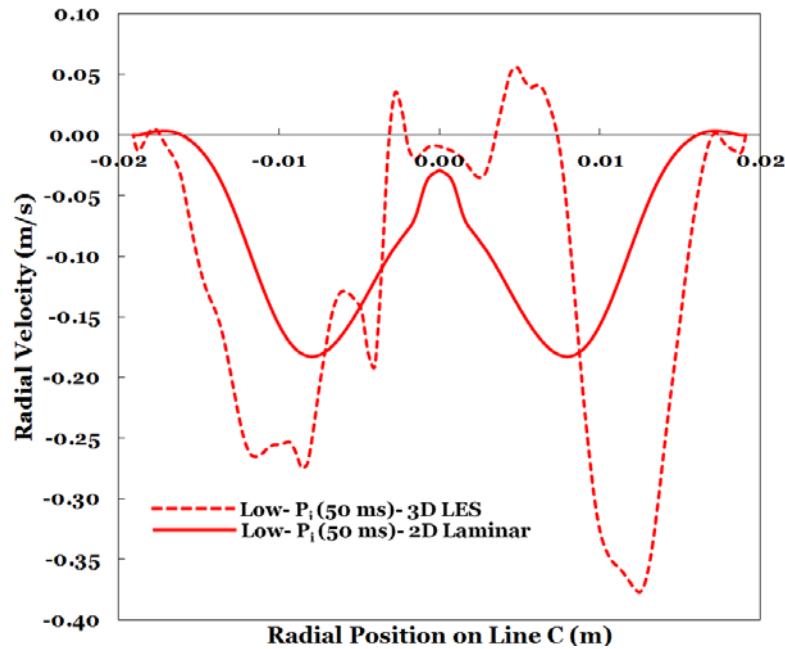


**Figure 16: Comparison of radial velocity distribution along line C using 2D laminar (solid lines) and LES (dashed lines) models at post-compression time of 50 for low-pressure condition.**

Figure 17 shows the radial distribution of temperature on line C close to the piston head for LES and 2D laminar cases at 50 ms and 200 ms post-compression times for the low initial pressure case. This figure shows that at both times the laminar model fails to predict temperature fluctuations on this line. At 50 ms post-compression time the temperature magnitude for laminar case is close to LES model, but at 200 ms post-compression time laminar model over-predict temperature magnitude over most points on line C. The predictions of laminar and LES models are completely different at 50 and 200 ms. Similar to high-pressure case, there is a uniform temperature distribution and considerable amount of under-prediction for the total temperature at the centerline for laminar model. Also, at 200 ms post-compression there is a

considerable over-prediction for the temperature distribution before the centerline position for laminar case.

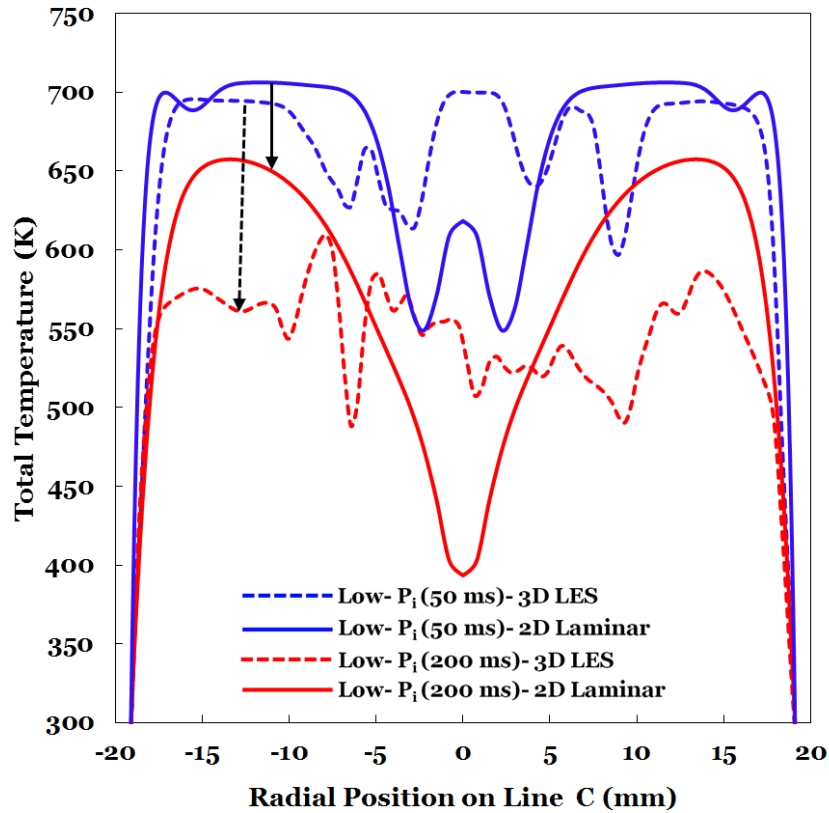


**Figure 17: Comparison of computed temperature distribution along line C using 2D laminar (solid lines) and LES (dashed lines) models at post-compression times of 50 (blue lines) and 200ms (red lines) for low-pressure condition.**

### 3.3. Comparison of CFD Results and Correlation Prediction

In the authors' previous study [9], a correlation was developed to predict a temperature inhomogeneity parameter using a set of 2D laminar simulations.  $\bar{\varepsilon}$  represents the spatial average of temperature inhomogeneity  $\varepsilon$  over the whole main chamber and is defined in Equation (8).

$$\bar{\varepsilon}(t) = \frac{T_{max}(t) - \bar{T}(t)}{T_{max}(t) - T_w} \quad (8)$$

Where  $T_{max}(t)$  is the core gas temperature or maximum gas temperature in the main chamber,  $\bar{T}(t)$  is the mass-average temperature in the main chamber, and  $T_w$  is the wall temperature. A value of  $\bar{\varepsilon}$  close to 1 implies that  $\bar{T} \approx T_w$ , indicating that the bulk gas temperature is dominated by wall heat transfer, while  $\bar{\varepsilon}$  close to 0 implies that gas temperature everywhere is close to the core temperature, and thus wall effects are small [9]. The computational method to extract the correlation is described in detail in [9]. The form and values of the correlation are shown in below equations.

$$\bar{\varepsilon}_p(Pe, a, b, t^*) = \bar{\varepsilon}_{\infty p} - (\bar{\varepsilon}_{\infty p} - \bar{\varepsilon}_{0p})e^{-\beta t^*} \quad (9)$$

$$\beta = 3.08Pe^{-0.32}a^{-0.08}b^{-0.4} \quad (10)$$

$$\bar{\varepsilon}_{0p} = 1.49Pe^{-0.47}a^{-0.07}b^{-0.63} \quad (11)$$

$$\bar{\varepsilon}_{\infty p} = 1.66Pe^{-0.22}b^{-0.33} \quad (12)$$

In the above equation, subscript  $p$  denotes prediction based on correlation of the computational results. Temperature inhomogeneity parameters  $\bar{\varepsilon}_{0p}$  and  $\bar{\varepsilon}_{\infty p}$  are predicted values at the end of compression ( $t^* = 0$ ) and the asymptotic final state ( $t^* \rightarrow \infty$ ), respectively.  $Pe$  is Peclet number,  $a$  is crevice volume ratio,  $b$  is aspect ratio and  $t^*$  is dimensionless post-compression time. The equations of these parameters are defined as follows:

$$Pe = Re_S Pr \quad (13)$$

$$a = \frac{4V_{cr}}{\pi D^2 S} \quad (14)$$

$$b = \frac{D}{2S} \quad (15)$$

$$t^* = \frac{t - t_c}{t_c} \quad (16)$$

In the above relations,  $Re_S$  is Reynolds number based on stroke length,  $Pr$  is Prandtl number,  $V_{cr}$  is crevice volume,  $D$  is main chamber diameter,  $t$  is time and  $t_c$  is EOC time.

The main purpose of developing a correlation is to enable approximation of temperature inhomogeneity using simple engineering calculations without having to resort to expensive experimental measurement and/or CFD simulations. The correlation can be used to design an experimental campaign that avoids conditions likely to cause non-uniform ignition. It can also be used to guide and assess crevice designs for previously unstudied conditions and gas mixtures. The temperature inhomogeneity parameters computed by 2D laminar and 3D LES CFD results are compared to that predicted by the correlation. For initial pressure of 50 kPa and temperature of 298 K, four LES simulations and four 2D laminar simulations are conducted for minimum, average and maximum Peclet numbers. The values of reference, minimum, average and maximum Peclet numbers are shown in Table 3. As stated in the previous study [9], these values represent the minimum, average and maximum possible of Peclet numbers for a wide range of available RCMs in the literature. Note that  $a$  and  $b$  are fixed values since this study focuses solely on the current NUI Galway RCM and crevice designs. These reference values are presented in Table 3.

The results predicted by 2D laminar and 3D LES CFD simulations and the correlation are shown and compared in Figure 18. As predicted in the previous study [9], the results show that for minimum  $Pe$ , temperature inhomogeneity is maximum and for maximum  $Pe$ , temperature

inhomogeneity is minimum, during all post-compression times. The results show that for all  $Pe$  there is satisfactory agreement between 2D laminar and 3D LES results especially for long post-compression times. As described in [9], the correlation is able to predict the temperature inhomogeneity parameter within a  $\pm 20\%$  tolerance of 2D laminar CFD results for most cases. According to this figure, for minimum, maximum and reference  $Pe$ , the predicted inhomogeneity parameter using the correlation satisfies this tolerance. For average  $Pe$ , the correlation can predict the trend of CFD results. These findings indicate the following: (1) 2D laminar and 3D LES CFD simulations produce very similar predictions of temperature inhomogeneity at high pressures, (2) basing the correlation for temperature inhomogeneity on computationally expensive 3D LES results rather than cheaper 2D laminar predictions would have negligible impact on correlation predictions.

**Table 3. Minimum, geometric average and maximum possible values of each dimensionless parameter based on a wide range of available RCMs used in the parametric study [9]. Note that  $a$  and  $b$  are fixed at the reference values for the simulations in Figure 18 since this study focuses solely on the RCM and crevice design of current NUI Galway RCM and crevice designs.**

Dimensionless Parameter	Reference	Minimum	Average	Maximum
$Re_S$	$2.128 \times 10^5$	$0.100 \times 10^5$	$0.894 \times 10^5$	$8.000 \times 10^5$
$Pr$	0.728	0.15	0.500	0.85
$Pe$	$1.549 \times 10^5$	$0.015 \times 10^5$	$0.447 \times 10^5$	$6.800 \times 10^5$
$a$	0.012	0.004	0.020	0.009
$b$	0.114	0.070	0.200	0.118

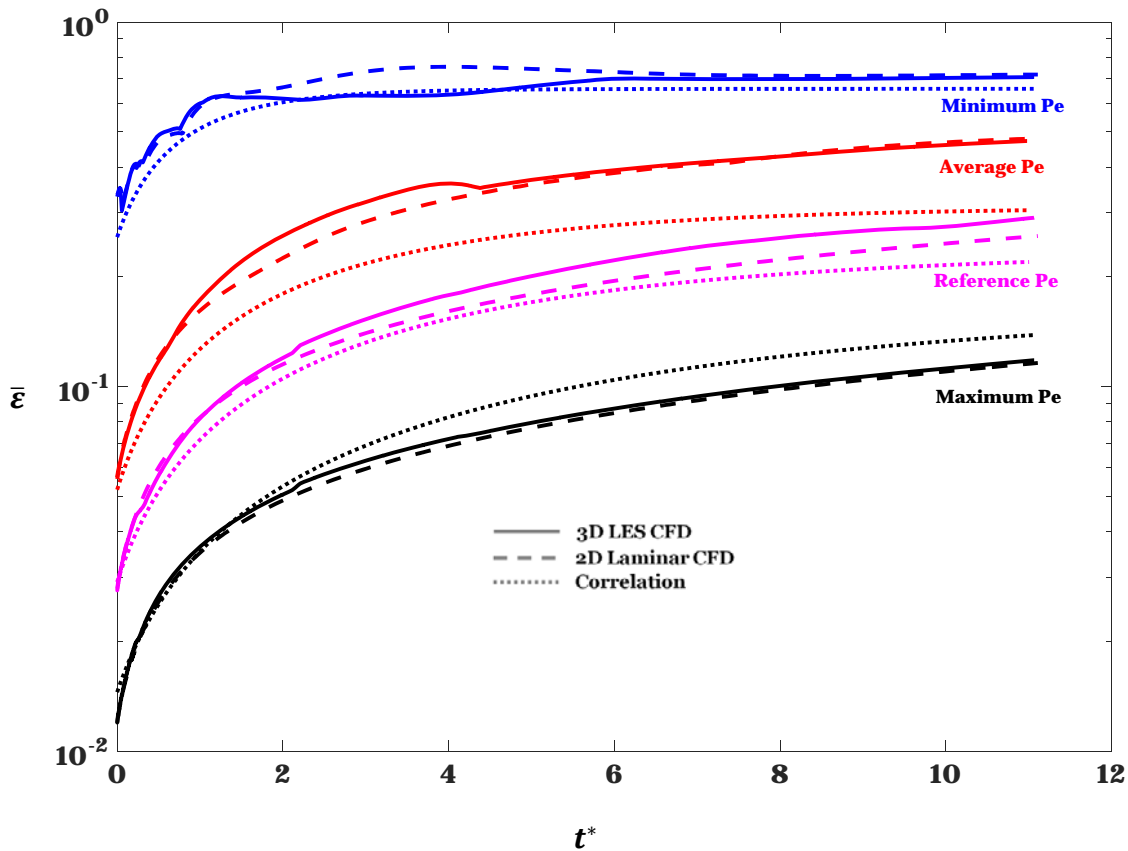


Figure 18: Comparison of computed temperature inhomogeneity parameter using LES and 2D laminar CFD, and that predicted using the correlation [9].  $\bar{\epsilon}$  is the average temperature inhomogeneity parameter defined in Eq. 7, and  $t^*$  is dimensionless post-compression time defined in Eq. 14. Solid lines represent 3D LES CFD results, dashed lines are 2D laminar CFD and dotted lines are predicted results by correlation.  $t_c = 18 \text{ ms}$ ,  $P_i = 50 \text{ kPa}$ ,  $T_i = 298 \text{ K}$ ,  $a = 0.012$  and  $b = 0.114$ .

#### 4. Conclusions

A set of CFD simulations is presented in this study to develop a framework for RCM testing campaigns and validate performance of a previously-developed correlation for temperature inhomogeneity in RCMs at different conditions. The flow field inside the main chamber of the

NUI Galway RCM is characterized at different initial pressures using 3D LES simulations and the results are compared with 2D laminar CFD results. The temperature inhomogeneity parameter during post-compression times in the main chamber is computed and compared using 3D LES, 2D laminar and a previously-developed correlation [9].

The results show that the current NUI Galway crevice has a satisfactory ability during compression to suppress the roll-up vortex at the high-pressure condition. As a result, there is no vortex on the piston face at the end of compression. During the post-compression period, there is therefore a uniform temperature field inside the main chamber, with only a few small eddies appearing at long post-compression times. At this condition in which the crevice is able to suppress the roll-up vortex, the 2D laminar CFD model is able to effectively predict compression and post-compression flow field in comparison with LES model. For the low-pressure condition, the crevice fails to fully absorb the boundary layer gas. There is therefore a remaining vortex inside the main chamber on the piston face, which generates irregular flow structures and turbulent eddies during the post-compression period. As a result, there is a need to modify the crevice configuration in this condition to prevent the formation of the roll-up vortex. Furthermore, the results show that the previously-developed correlation [9] is able to predict the computed results of 3D LES for the temperature inhomogeneity parameter within a  $\pm 20\%$  in most cases.

A computationally-efficient framework is proposed for RCM testing consisting of the following steps: (1) select required in-chamber test conditions, (2) list all possible RCM, crevice, diluent and initial condition configurations that can reach the test conditions, (3) use the

correlation to eliminate those configurations that produce unacceptable temperature inhomogeneity, (4) use 2D laminar simulations of some or all of the acceptable configurations to further eliminate configurations predicted to produce roll-up vortices, (5) use 3D LES simulations of some or all of these remaining configurations to gain further confidence that roll-up vortices are not formed.

Future works will focus on development of experimental studies using particle image velocimetry (PIV) technique and DNS to fundamentally understand the fluid dynamic processes and measure the velocity field inside the main chamber of the NUI Galway RCM. The results will be used to validate LES simulations. A range of crevice configurations will be designed to cover a wide range of operating conditions using a systematic optimization method coupled with the correlation or 2D laminar simulations. Furthermore, the impact of non-ideal operating conditions, including piston timing and conjugate heat transfer culminating in reactive flow simulation under completely realistic conditions will be studied to improve the simulation setup.

### **Acknowledgments**

This study is supported by an NUI Galway College of Engineering and Informatics Scholarship and by Science Foundation Ireland and Gas Networks Ireland through the Research Centre for Marine and Renewable Energy in Ireland (MaREI) under grant number 12/RC/2302. Computational facilities, software licences and technical support were provided through a Class B project award from the the DJEI/DES/SFI/HEA-backed Irish Centre for High-End Computing (ICHEC).

## References

- [1] Würmel, J., Silke, E. J., Curran, H. J., Ó Conaire, M. S., and Simmie, J. M., 2007, “The effect of diluent gases on ignition delay times in the shock tube and in the rapid compression machine,” *Combust. Flame*, 151(1–2), pp. 289–302.
- [2] S. Scott Goldsborough, Simone Hochgreb, Guillaume Vanhove, Margaret S. Wooldridge, Henry J. Curran, C.-J. S., 2017, “Advances in rapid compression machine studies of low- and intermediate-temperature autoignition phenomena,” *Prog. Energy Combust. Sci.*, 63, pp. 1–78.
- [3] Lee, D., and Hochgreb, S., 1998, “Rapid compression machines: Heat transfer and suppression of corner vortex,” *Combust. Flame*, 114(3–4), pp. 531–545.
- [4] Würmel, J., and Simmie, J. M., 2005, “CFD studies of a twin-piston rapid compression machine,” *Combust. Flame*, 141(4), pp. 417–430.
- [5] Mittal, G., and Sung, C. J., 2006, “Aerodynamics inside a rapid compression machine,” *Combust. Flame*, 145(1–2), pp. 160–180.
- [6] Mittal, G., Raju, M. P., and Sung, C. J., 2010, “CFD modeling of two-stage ignition in a rapid compression machine: Assessment of zero-dimensional approach,” *Combust. Flame*, 157(7), pp. 1316–1324.

- [7] Mittal, G., Raju, M. P., and Sung, C. J., 2012, “Vortex formation in a rapid compression machine: Influence of physical and operating parameters,” *Fuel*, 94, pp. 409–417.
- [8] Mittal, G., and Chomier, M., 2014, “Effect of crevice mass transfer in a rapid compression machine,” *Combust. Flame*, 161(2), pp. 398–404.
- [9] Yousefian, S., Gauthier, F., Morán-Guerrero, A., Richardson, R. R., Curran, H. J., Quinlan, N. J., and Monaghan, R. F. D., 2015, “Simplified Approach to the Prediction and Analysis of Temperature Inhomogeneity in Rapid Compression Machines,” *Energy & Fuels*, 29, p. 8216–8225.
- [10] Bourgeois, N., Goldsborough, S. S., Vanhove, G., Duponcheel, M., Jeanmart, H., and Contino, F., 2017, “CFD simulations of Rapid Compression Machines using detailed chemistry: Impact of multi-dimensional effects on the auto-ignition of the iso-octane,” *Proc. Combust. Inst.*, 36, pp. 383–391.
- [11] Ben-Houidi, M., Sotton, J., Claverie, A., Strozzi, C., and Bellenoue, M., 2016, “Application of high-speed PIV and Toluene PLIF techniques to study aerodynamics and thermal stratification inside a flat piston Rapid Compression Machine,” 18th International Symposium on the Application of Laser and Imaging Techniques to Fluid Mechanics, LISBON.
- [12] Banaeizadeh, A., 2010, “Large-Eddy Simulation Of Turbulent Flows In Internal Combustion Engines,” PhD thesis, Mechanical Engineering department, Michigan State University.

- [13] Lodier, G., Merlin, C., Domingo, P., Vervisch, L., and Ravet, F., 2012, “Self-ignition scenarios after rapid compression of a turbulent mixture weakly-stratified in temperature,” *Combust. Flame*, 159(11), pp. 3358–3371.
- [14] Guibert, P., Keromnes, A., and Legros, G., 2010, “An experimental investigation of the turbulence effect on the combustion propagation in a rapid compression machine,” *Flow, Turbul. Combust.*, 84(1), pp. 79–95.
- [15] Schmitt, M., Frouzakis, C. E., Wright, Y. M., Tomboulides, A. G., and Boulouchos, K., 2015, “Direct numerical simulation of the compression stroke under engine-relevant conditions: Evolution of the velocity and thermal boundary layers,” *Int. J. Heat Mass Transf.*, 91, pp. 948–960.
- [16] Schmitt, M., Frouzakis, C. E., Tomboulides, A. G., Wright, Y. M., and Boulouchos, K., 2015, “Direct numerical simulation of the effect of compression on the flow, temperature and composition under engine-like conditions,” *Proc. Combust. Inst.*, 35(3), pp. 3069–3077.
- [17] Schmitt, M., Frouzakis, C. E., Wright, Y. M., Tomboulides, A. G., and Boulouchos, K., 2016, “Investigation of wall heat transfer and thermal stratification under engine-relevant conditions using DNS,” *Int. J. Engine Res.*, 17(1), pp. 63–75.
- [18] Schmitt, M., Frouzakis, C. E., Wright, Y. M., Tomboulides, A., and Boulouchos, K., 2016, “Direct numerical simulation of the compression stroke under engine relevant conditions: Local wall heat flux distribution,” *Int. J. Heat Mass Transf.*, 92, pp. 718–731.

- [19] Morse, A. P., Whitelaw, J. H., and Yianneskis, M., 1979, “Turbulent Flow Measurements by Laser-Doppler Anemometry in Motored Piston-Cylinder Assemblies,” *J. Fluids Eng.*, 101, pp. 208–216.
- [20] Mandanis, C., Schmitt, M., Koch, J., Wright, Y. M., and Boulouchos, K., 2018, “Wall Heat Flux and Thermal Stratification Investigations during the Compression Stroke of an engine-like Geometry: A comparison between LES and DNS,” *Flow, Turbul. Combust.*, 100(3), pp. 769–795.
- [21] Grogan, K. P., Scott Goldsborough, S., and Ihme, M., 2015, “Ignition regimes in rapid compression machines,” *Combust. Flame*, 162(8), pp. 3071–3080.
- [22] Ihme, M., 2012, “On the role of turbulence and compositional fluctuations in rapid compression machines: Autoignition of syngas mixtures,” *Combust. Flame*, 159(4), pp. 1592–1604.
- [23] Pope, S. B., 2000, *Turbulent Flows*, Cambridge University Press.
- [24] Sheng, C., 2017, “Transition Prediction,” *Advances in Transitional Flow Modeling*, Springer, pp. 9–19.
- [25] Smagorinsky, J., 1963, “General Circulation Experiments With the Primitive Equations,” *Mon. Weather Rev.*, 91(3), pp. 99–164.
- [26] Kim, S., 2004, “Large Eddy Simulation Using an Unstructured Mesh Based Finite-Volume Solver,” AIAA-2004-2548. 34th Fluid Dynamics Conference and

Exhibit American Institute of Aeronautics and Astronautics.

- [27] Kim, W., Kim, W., and Menon, S., 1997, “Application of the localized dynamic subgrid-scale model to turbulent wall-bounded flows,” AIAA-97-0210. 35th Aerospace Sciences Meeting, Reno, NV American Institute of Aeronautics and Astronautics.
- [28] P.J. Linstrom and W.G. Mallard, E., 2017, “NIST Chemistry WebBook, NIST Standard Reference Database Number 69,” Natl. Inst. Stand. Technol. Gaithersbg. MD, 20899, doi10.18434/T4D303.
- [29] Pope, S. B., 2004, “Ten questions concerning the large-eddy simulation of turbulent flows,” *New J. Phys.*, 6(35).
- [30] di Mare, F., Knapstein, R., and Baumann, M., 2014, “Application of LES-quality criteria to internal combustion engine flows,” *Comput. Fluids*, 89, pp. 200–213.
- [31] Wang, T., Zhang, X., Xu, J., Zheng, S., and Hou, X., 2015, “Large-eddy simulation of flame-turbulence interaction in a spark ignition engine fueled with methane/hydrogen/carbon dioxide,” *Energy Convers. Manag.*, 104, pp. 147–159.
- [32] Bottone, F., Kronenburg, A., Gosman, D., and Marquis, A., 2012, “Large Eddy Simulation of diesel engine in-cylinder flow,” *Flow, Turbul. Combust.*, 88(1–2), pp. 233–253.
- [33] Wang, T., Li, W., Jia, M., Liu, D., Qin, W., and Zhang, X., 2015, “Large-eddy simulation of in-cylinder flow in a DISI engine with charge motion control valve: Proper orthogonal

- decomposition analysis and cyclic variation,” *Appl. Therm. Eng.*, 75, pp. 561–574.
- [34] Goryntsev, D., Sadiki, A., Klein, M., and Janicka, J., 2009, “Large eddy simulation based analysis of the effects of cycle-to-cycle variations on air-fuel mixing in realistic DISI IC-engines,” *Proc. Combust. Inst.*, 32 II(2), pp. 2759–2766.
- [35] Park, P., and Keck, J. C., 1990, “Rapid Compression Machine Measurements of Ignition Delays for Primary Reference Fuels,” SAE Technical Paper Series 900027.